Available online at www.sciencedirect.com

ScienceDirect

Underground Space 15 (2024) 113–130

www.keaipublishing.com/undsp

Research Paper

Dynamic response of water-rich tunnel subjected to plane P wave considering excavation induced damage zone

Gongliang Xiang [a], Ming Tao [a,*], Rui Zhao [a], Huatao Zhao [b], Muhammad Burhan Memon [a], Chengqing Wu [c]

[a] School of Resources and Safety Engineering, Central South University, Changsha 410083, China
[b] School of Geoscience and Technology, Southwest Petroleum University, Chengdu 610500, China
[c] School of Civil and Environmental Engineering, University of Technology Sydney, NSW 2007, Australia

Received 20 May 2023; received in revised form 9 August 2023; accepted 15 August 2023
Available online 26 September 2023

Abstract

The stability analysis of a deep buried tunnel subjected to dynamic disturbance is an important issue. In this study, the transient response has been obtained by establishing a water-rich tunnel model considering excavation damage zone (EDZ). Based on Biot's two-phase dynamic theory and wave function expansion method, the analytical solution of dynamic response around the water-rich tunnel containing EDZ subjected to P wave is derived. Moreover, Fourier transform and Duhamel's integral technique is introduced to calculate the transient response, and the equivalent blasting curve is adopted to input excitation function. The dimensionless parameters thickness N and shear modulus ratio $\widetilde{\mu}$ are defined to characterize the degree of damage in the surrounding rock, investigating the influencing factors, such as the parameters and the incident source frequencies. The results indicate that the dynamic stress concentration factor (DSCF) gradually decreases as the dimensionless parameters increase. Additionally, it is observed that the DSCF is more sensitive to changes in the thickness parameter N. Finally, the influence of the waveform parameters has been taken into account in the analysis of transient response, and the stress state and transfer process in each time stage of the EDZ are analyzed. This study establishes a theoretical foundation for comprehending the mechanical behavior and support design considerations associated with a deep-buried water-rich tunnel containing EDZ.

Keywords: Water-rich tunnel; Two-phase dynamic theory; Wave scattering; Transient response; Dynamic stress concentration

1 Introduction

With the increase in demand of mineral resources and subsequent decrease in the shallow mineral resources, it needs time to exploit mineral resources deep down the earth by the construction of tunnels. However, with this increase in depth, deep rock mass is in the complex environment condition of the high in situ stress and intensive excavation disturbances (Feng et al., 2018; Luo et al., 2023; Xu et al., 2022; Zhou et al., 2023; Zhao et al., 2023a, 2023b). Excavation in this environment will cause stress redistribution and damage around an underground opening, known as excavation damaged zone (EDZ) (Lai et al., 2021; Martino & Chandler, 2004; Yan et al., 2015). The study of EDZ has a significant impact on preventing geology casualty and safety excavation. Meanwhile, dynamic disturbances such as blasting and earthquake further lead to damage and instability of deep underground structures, and the investigation of such problems can focus on the scattering of stress waves on the periphery of the deep tunnels (Li et al., 2014; Li & Weng, 2016; Su et al., 2017; Tao et al., 2013; Zhao et al., 2023a, 2023b). Therefore, the mechanical characteristics of tunnel with EDZ subjected to dynamic disturbance could be a significant prerequisite for designing the support and safe operation in underground space.

* Corresponding author.
E-mail address: mingtao@csu.edu.cn (M. Tao).

https://doi.org/10.1016/j.undsp.2023.08.010

Excavation-induced stress redistribution and the back-pressure on the rock deformation by the emplacement of the rock support are gradually considered as the main factors (Read, 2004; Tsang et al., 2005). According to the existing theoretical research status, the Hoek-Brown (H-B) criterion has been widely recognized and applied (Brown, 1980). Moreover, elasto-plastic approaches are commonly used in some research studies to derive the analytical solution of EDZ for elastic-brittle-plastic assumption (Brown et al., 1983). Mitaim and Detournay (2004) introduced the sliding/wing crack model into the problem of a circular hole with EDZ in the rock mass subjected to hydrostatic stress by assuming the rock mass containing a uniform initial distribution of microcracks. Bobet (2009) obtained an exact solution for a deep buried circular tunnel in cylindrical anisotropy rock mass based on elastic assumption. In addition, the influence of rock properties on rockbolts, the effect of EDZ on the displacement and the stresses around the tunnel were analyzed. On the other hand, Kaiser et al. (2001) investigated the process of excavation-induced stress change and the types of rock mass failure at Winston Lake Mine by using four CSIRO HI stress cells. When the drilling and blasting (D & B) method was widely adopted to roadways excavation, the intensive disturbance was considered as a non-negligible factor (Yin et al., 2022). The EDZ caused by explosion and mechanical excavation or stress redistribution was analyzed respectively according to numerous observations of practical testing by Siren et al. (2015). Although some significant research results have been found about the evolution process and mechanical mechanism of EDZ, there were still some issues for analyzing on the vibration reduction in existing tunnel containing EDZ, which attract little attention.

The study on the damage induced underground structures by dynamic disturbance such as blasting and earthquake can be found decades ago, and it can be explained in the theory of the scattering of stress waves on the underground structure (Tao et al., 2023b; Zhao et al., 2023a, 2023b). Various research studies have been done such as problems of the scattering of elastic waves on a circular hole and sphere are performed by Mow and Pao (1971), and the wave function expansion method is proposed to study the scattering of stress waves around a circular hole along with other methods summarized in monograph. Recently, Zhao et al. (2023a, 2023b) presented the dynamic response around a circular hole using this method and the relationship between transient response and waveform parameters was investigated based on Fourier transform method. In most of the cases, it is found that the inner defects of rock mass and roadway section are not round. The expression of dynamic stress concentration around an elliptical hole or inclusion subjected to plane SH wave can be derived based on the Mathieu equation (Tao et al., 2023a, 2020b). With the rapid development of science and technology, numerical simulation and approximate solution methods are applied gradually in rock mechanical and rock engineering. The propagation process and law of stress wave in rock mass with a hole and the mode of failure around the hole can be obtained by establishing a three-dimension model (Li et al., 2018; Li & Weng, 2016; Tao et al., 2023b, 2020a). Most studies demonstrated that dynamic response in rock mass could be associated with waveform and physical and mechanical parameters. In addition, numerous underground space constructions were in water-rich environments and the interaction between fluid and rock soil mass under the action of stress wave must be taken into account (Gu et al., 2023). After the constitutive theory of saturated porous media was presented by Biot (1956a, 1956b), there were several research results on dynamic analysis of water-rich rock and soil that were considered as saturated porous media (Hasheminejad & Avazmohammadi, 2007; Jiang et al., 2009; Li et al., 2022; Senjuntichai & Rajapakse, 1993; Xu et al., 2006). To summarize the above, the study results of the formation and evolutionary mechanism of EDZ, and the dynamic response of underground structures subjected to stress wave were very abundant. Unfortunately, these studies mainly focused on the dynamic response around a cavity subjected dynamic disturbance, and the mechanical characteristics of EDZ under static loading. The mechanical behavior and dynamic response of underground roadway with EDZ in water-rich environments has not yet been fully investigated.

The objective of this paper is to investigate the dynamic response of an underground circular tunnel with EDZ subjected to a plane P wave scattering in water-rich environments. The distribution of dynamic stress concentration in EDZ subjected to a plane P wave has been analyzed by adopting wave function expansion method and introducing the amended Biot model (Biot, 1956a, 1956b). The analytical solution of transient response is derived from Fourier transform. The influence of the buried depth of the tunnel containing EDZ on the distribution of stress is investigated and the results for transient response with different periods and times were given. The results of this study provide a theoretical basis in supporting underground tunnels and the safety of engineering excavation.

2 Model and governing equations of the problem

2.1 Model

The model of EDZ is generated around a deep buried circular cavity under the influence of in-situ stress, as shown in Fig. 1. Based on the classical elastic theory, the EDZ produced by the circular tunnel under the hydrostatic stress σ_0 is also circular (Mitaim & Detournay, 2004). The size of EDZ is generally one to three times as large as the radius of the tunnel according to theory and engineering field testing. The influence of the environment of water-rich on the cavity is taken into account, whereas the permeability of rock in EDZ is higher than that in intact rock mass outside (Cho et al., 2013), and fluid penetrates remove

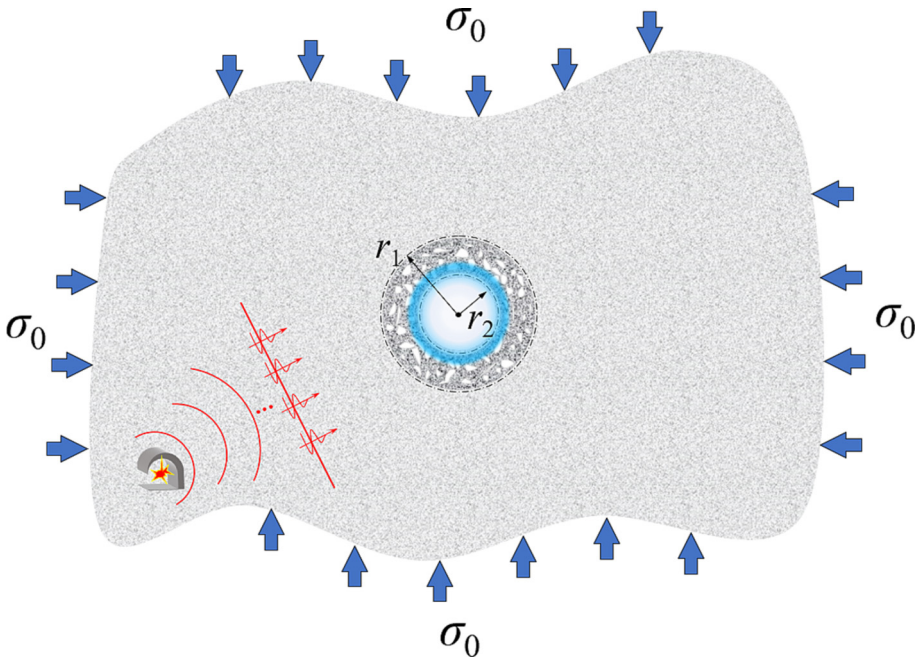

Fig. 1. Circular tunnel subjected to a hydrostatic stress field.

more easily into fractures of the surrounding rock in a water-rich underground tunnel containing EDZ. Consequently, the EDZ can be considered as a saturated porous elastic medium, and outside intact rock mass can be considered as an elastic medium in this investigation. Fluid can more easily penetrate into fractures of the surrounding rock in a water-rich underground tunnel containing EDZ. Consequently, the mediums in the model can be defined as follows: the EDZ is considered a saturated porous elastic medium, while the outside intact rock mass is treated as an elastic medium in this investigation. Furthermore, it is essential to consider the influence of dynamic disturbance such as blasting or machine excavation on a tunnel that contains the EDZ as depicted in Fig. 1. The dynamic disturbance is simplified as a plane P wave incidence. To summarize the points mentioned above, the structure of theoretical model is depicted in Fig. 2. The fluid-saturated medium is simulated by Biot's two-phase theory, and both of this material and the elastic medium are homogenous, isotropic, and linearly elastic (Biot, 1956a, 1956b). The inner radius of the tunnel is r_2 and the outer radius of the EDZ is r_1. The material properties of the surrounding rock are the Lame constants λ_1 and μ_1, the Poisson's ratio v_1, and the density ρ_1, respectively.

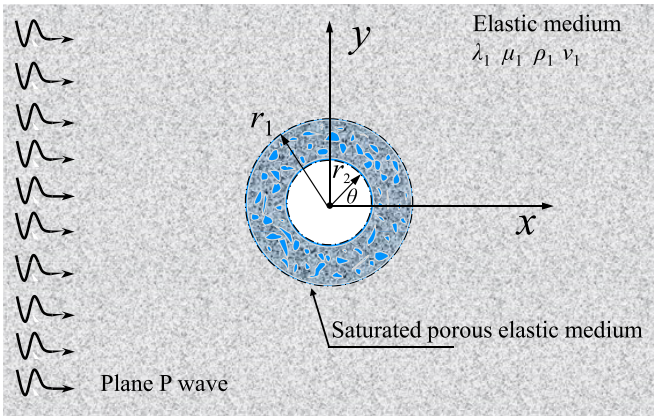

Fig. 2. The circular tunnel containing EDZ in the elastic medium by plane P wave.

2.2 Biot's theory for the saturated porous elastic medium

Based on Biot's wave motion theory, the equation of motion for EDZ as a saturated porous elastic material can be expressed as follows (Biot, 1956a, 1956b):

$$\begin{cases} \mu u_{i,jj} + (\lambda_2 + \alpha^2 M + \mu_2) u_{j,ji} + \alpha M w_{j,ji} = \rho u_i + \rho_f w_i \\ \alpha M u_{j,ji} + M w_{j,ji} = \rho_f u_i + m w_i + b w_i \end{cases}, \quad (1)$$

where u_i and w_i denote the displacement of solid and the relative displacement of pore-fluid, respectively; λ_2, μ_2, α, and M denote Biot's constants of solid phase; $\rho = f\,\rho_f + (1 - f)\rho_s$, where ρ and f denote the whole density and porosity of the saturated porous elastic medium respectively; ρ_f and ρ_s are the density of pore fluid and solid particles; $m = \rho_f / f$, $b = \eta / k_f$, where η and k_f are the viscidity and hydraulic conductivity of pore fluid respectively (Xu et al., 2006).

The constitutive relation of the saturated medium is:

$$\begin{cases} \sigma_{ij} = \lambda_2 \delta_{ij} e + 2\mu_2 \gamma_{ij} - \alpha \delta_{ij} p_f \\ p_f = -\alpha M e + M \zeta \end{cases}, \quad (2)$$

where σ_{ij} denotes the whole stress and p_f is the pressure of pore fluid; γ_{ij} denotes the strain tensor; δ_{ij} is Kronecker delta; $e = u_{ij}$ and $\zeta = -w_{ij}$, where e denotes the volume strain and ζ is the volume of fluid injection into unit volume of bulk material.

According to Helmholtz decomposition theorem, the displacement of the solid phase and the relative displacement of the fluid phase can be expressed by vector and scalar as:

$$\begin{cases} u = \nabla\varphi + \nabla \times \psi \\ w = \nabla\chi + \nabla \times \Theta \end{cases}, \tag{3}$$

where φ and ψ denote the vector potential function and scalar potential function of the solid phase respectively; ∇ denotes the gradient operator; χ and Θ are potential function of the fluid phase.

The decomposition expression can be obtained by substituting Eq. (3) into Eq. (1):

$$\begin{cases} \begin{bmatrix} \lambda_2 + \alpha^2 M + 2\mu_2 & \alpha M \\ \alpha M & M \end{bmatrix} \begin{bmatrix} \nabla^2\varphi \\ \nabla^2\chi \end{bmatrix} = \begin{bmatrix} -\rho_b\omega^2 & -\rho_f\omega^2 \\ -\rho_f\omega^2 & -m\omega^2 + i\omega b \end{bmatrix} \begin{bmatrix} \varphi \\ \chi \end{bmatrix} \\ \begin{bmatrix} \mu_2 & 0 \\ 0 & 0 \end{bmatrix} \begin{bmatrix} \nabla^2\psi \\ 0 \end{bmatrix} = \begin{bmatrix} -\rho_b\omega^2 & -\rho_f\omega^2 \\ -\rho_f\omega^2 & -m\omega^2 + i\omega b \end{bmatrix} \begin{bmatrix} \psi \\ \Theta \end{bmatrix} \end{cases}. \tag{4}$$

Furthermore, the following Helmholtz equation can be obtained (Hasheminejad & Avazmohammadi, 2007):

$$\begin{cases} \nabla^2\varphi_2^{p(1,2)} + \alpha_{2(1,2)}^2\varphi_2^{p(1,2)} = 0 \\ \nabla^2\psi + \beta_2^2\psi = 0 \end{cases}, \tag{5}$$

where ∇^2 is the Laplace operator; $\varphi_2^{p(1,2)}$, ψ represent three potentials accounting for fast compression (P_1), slow compression (P_2) and shear wave (SV) respectively; $\alpha_{2(1,2)}$,β_2 are the complex wave numbers of the fast/slow compression and shear wave, and their expression can be written as (Xu et al., 2006):

$$\alpha_{2(1,2)}^2 = \frac{B \mp \sqrt{B^2 - 4AC}}{2A},$$
$$\beta_2^2 = \frac{C}{D}, \begin{cases} A = (\lambda_2 + 2\mu_2)M \\ B = (\lambda_2 + \alpha^2 M + 2\mu_2)\cdot(m\omega^2 - ib\omega) + \rho\omega^2 M - 2\rho_f\omega^2\alpha M \\ C = \rho\omega^2(m\omega^2 - i\omega b) - \rho_f\omega^4 \\ D = \mu_2(m\omega^2 - i\omega b) \end{cases}, \tag{6}$$

where ω denotes the circular frequency; i denotes the imaginary unit.

3 Wave field in different mediums

3.1 Total wave field in the intact rock mass

It is assumed that an incident P wave propagates in the intact rock mass (i.e., in a whole elastic space) and passes through the circular tunnel containing EDZ. Based on wave function expansion methods, the incident P wave in the intact rock mass can be expressed as (Tao et al., 2020a):

$$\varphi_r^i = \varphi_0 \sum_{n=0}^{\infty} \varepsilon_n i^n J_n(\alpha_1 r_1)\cos n\theta \cdot e^{-i\omega t}, \tag{7}$$

where φ_0 denotes the amplitude of the incident wave; $\varepsilon_n = 1$ when $n = 0$, and $\varepsilon_n = 2$ when $n \geq 1$; J_n denotes the Bessel function of the first kind of integer order n; α_1 is the compression wave number in the elastic medium; θ and $e^{-i\omega t}$ are the angle and time factor, respectively.

The presence of the interface between EDZ and intact rock mass results in two reflected waves when the incident P wave meets the interface. The reflected waves are P wave and SV wave and they can be expressed as:

$$\begin{cases} \varphi_r^P = \sum_{n=0}^{\infty} A_n H_n^{(1)}(\alpha_1 r_1)\cos n\theta \cdot e^{-i\omega t} \\ \phi_r^{SV} = \sum_{n=0}^{\infty} B_n H_n^{(1)}(\beta_1 r_1)\sin n\theta \cdot e^{-i\omega t} \end{cases}, \tag{8}$$

where A_n and B_n are unknown coefficients to be determined later; $H_n^{(1)}$ denotes the Hankel function of the first kind of integer order n; β_1 denotes the wave number of shear wave in the intact rock mas. Thus, the total wave fields in intact rock mass are $\varphi_r = \varphi_r^i + \varphi_r^P$, and $\phi_r = \phi_r^{SV}$.

3.2 Total wave field in EDZ

The refracted waves will be generated in EDZ (i.e., in the saturated porous elastic medium), when the incident P wave meets the interface of the intact rock mass and the EDZ. According to Huygens Principle (Pao et al., 1973), the refracted waves can be considered as the infrasonic sources which are diverging waves generally. Furthermore, the refracted waves will scatter once more when that meets the wall of the circular tunnel, and the new scattering waves can be considered as converging waves. Consequently, in the region of EDZ $r_2 \leq r \leq r_1$, the total wave field can be expressed by standing waves which are formed of the diverging and converging waves.

Based on the wave function expansion methods, the wave field in the solid phase can be written in the form:

$$\begin{cases} \varphi_2^{p1} = \sum_{n=0}^{\infty} \left(C_n H_n^{(1)}(\alpha_{21} r) + D_n H_n^{(2)}(\alpha_{21} r)\right)\cos n\theta \cdot e^{-i\omega t} \\ \varphi_2^{p2} = \sum_{n=0}^{\infty} \left(E_n H_n^{(1)}(\alpha_{22} r) + F_n H_n^{(2)}(\alpha_{22} r)\right)\cos n\theta \cdot e^{-i\omega t} \\ \psi_s = \sum_{n=0}^{\infty} \left(M_n H_n^{(1)}(\beta_2 r) + N_n H_n^{(2)}(\beta_2 r)\right)\sin n\theta \cdot e^{-i\omega t} \end{cases}, \tag{9}$$

where $H_n^{(2)}$ denotes the Hankel function of the second kind of integer order n and C_n,⋯, N_n are unknown coefficients similar to A_n.

Likewise, the wave fields in the fluid phase are:

$$\varphi_f^{p1} = \xi_1 \cdot \varphi_2^{p1}, \varphi_f^{p2} = \xi_2 \cdot \varphi_2^{p2}, \psi_f = \xi_s \cdot \psi_s, \tag{10}$$

where ξ_1, ξ_2, ξ_s denote proportionality coefficients and these can be expressed as:

$$\xi_{1,2}=\frac{-(\lambda_2+\alpha^2M+2\mu_2)\alpha_{2(1,2)}^2+\rho\omega^2}{\alpha M\alpha_{2(1,2)}^2-\rho_f\omega^2},\ \xi_s=-\frac{\rho_f\omega^2}{m\omega^2-\mathrm{i}b\omega}. \tag{11}$$

4 Boundary conditions and detailed expressions of various components

4.1 Boundary conditions

In this case, EDZ around a deep buried circular tunnel was generated after excavating in a water-rich environment, and tractions, displacements and the pressure of pore fluid must be continuous at the interface. Thus, at $r=r_1$ and $r=r_2$, these continuous conditions can be expressed as:

$$\begin{cases} u_r^{(1)}=u_r^{(2)} \\ u_\theta^{(1)}=u_\theta^{(2)} \\ \sigma_{rr}^{(1)}=\sigma_{rr}^{(2)}\ (r=r_1), \\ \sigma_{r\theta}^{(1)}=\sigma_{r\theta}^{(2)} \\ w_f=0 \end{cases} \begin{cases} \sigma_{rr}^{(2)}=0 \\ \sigma_{r\theta}^{(2)}=0\ (r=r_2), \\ P_f=0 \end{cases} \tag{12}$$

where $u_r^{(1)}=u_r^{(2)}$ are the radial displacements and $\sigma_{rr}^{(1)}=\sigma_{rr}^{(2)}$ are the radial stresses; $u_\theta^{(1)}=u_\theta^{(2)}$ are the hoop displacements and $\sigma_{r\theta}^{(1)}=\sigma_{r\theta}^{(2)}$ are the hoop stresses; w_f is the displacement of pore fluid relative to the solid phase; P_f is the pressure of pore fluid.

4.2 Expressions of stress and displacement

Based on the relation among potential function, stress and displacement under cylindrical coordinates in rock mass can be expressed as (Yi et al., 2016):

$$\begin{cases} \sigma_{rr}^{(1)}=\lambda_1\Delta\varphi_1+2\mu_1\left[\frac{\partial^2\varphi_1}{\partial r^2}+\frac{\partial}{\partial r}\left(\frac{1}{r}\frac{\partial\phi}{\partial\theta}\right)\right] \\ \sigma_{\theta\theta}^{(1)}=\lambda_1\Delta\varphi_1+2\mu_1\left[\frac{1}{r}\left(\frac{\partial\varphi_1}{\partial r}+\frac{1}{r}\frac{\partial^2\phi}{\partial\theta^2}\right)+\frac{1}{r}\left(\frac{1}{r}\frac{\partial\phi}{\partial\theta}-\frac{\partial^2\phi}{\partial r\partial\theta}\right)\right], \\ \sigma_{\theta r}^{(1)}=\mu_1\left[2\left(\frac{1}{r}\frac{\partial^2\varphi_1}{\partial\theta\partial r}+\frac{1}{r^2}\frac{\partial\varphi}{\partial\theta}\right)+\left(\frac{1}{r^2}\frac{\partial^2\varphi_1}{\partial\theta^2}-r\frac{\partial}{\partial r}\left(\frac{1}{r}\frac{\partial\phi}{\partial\theta}\right)\right)\right] \end{cases}$$
$$\begin{cases} u_r^{(1)}=\frac{\partial\varphi_1}{\partial r}+\frac{1}{r}\frac{\partial\phi}{\partial\theta} \\ u_\theta^{(1)}=\frac{1}{r}\frac{\partial\varphi_1}{\partial\theta}-\frac{\partial\phi}{\partial r} \end{cases}. \tag{13}$$

Making use of Eqs. (1), (2) and the relationship between stress and displacement potential, the stress and displacement expressions of solid phase in EDZ (i.e., in a saturated porous elastic medium) can be derived to the following forms (Hasheminejad & Hosseini, 2002):

$$\begin{cases} \sigma_{rr}^{(2)}=\lambda_c\Delta\varphi_2+\alpha M\Delta\varphi_f+2\mu_2\left[\frac{\partial^2\varphi_2}{\partial r^2}+\frac{\partial}{\partial r}\left(\frac{1}{r}\frac{\partial\psi_s}{\partial\theta}\right)\right] \\ \sigma_{\theta\theta}^{(2)}=\lambda_c\Delta\varphi_2+\alpha M\Delta\varphi_f+2\mu_2\left[\frac{1}{r}\left(\frac{\partial\varphi_2}{\partial r}+\frac{1}{r}\frac{\partial^2\psi_s}{\partial\theta^2}\right)+\frac{1}{r}\left(\frac{1}{r}\frac{\partial\psi_s}{\partial\theta}-\frac{\partial^2\psi_s}{\partial r\partial\theta}\right)\right], \\ \sigma_{r\theta}^{(2)}=\mu_2\left[2\left(\frac{1}{r}\frac{\partial^2\varphi_2}{\partial\theta\partial r}+\frac{1}{r^2}\frac{\partial\varphi_2}{\partial\theta}\right)+\left(\frac{1}{r^2}\frac{\partial^2\varphi_2}{\partial\theta^2}-r\frac{\partial}{\partial r}\left(\frac{1}{r}\frac{\partial\psi_s}{\partial\theta}\right)\right)\right] \end{cases}$$
$$\begin{cases} u_r^{(2)}=\frac{\partial\varphi_2}{\partial r}+\frac{1}{r}\frac{\partial\psi_s}{\partial\theta} \\ u_\theta^{(2)}=\frac{1}{r}\frac{\partial\varphi_2}{\partial\theta}-\frac{\partial\psi_s}{\partial r} \end{cases}, \tag{14}$$

where $\lambda_c=\lambda_2+\alpha^2M$. Furthermore, the pore fluid pressure and the radial relative pore-fluid displacement of the fluid phase can be expressed as (Xu et al., 2006):

$$\begin{cases} -P_f=M(\Delta\varphi_f)+\alpha M(\Delta\varphi_s) \\ w_r=\frac{\partial\varphi_f}{\partial r}+\frac{1}{r}\frac{\partial\psi_f}{\partial\theta} \end{cases}. \tag{15}$$

As a result, introducing the potential functions into the formula for the displacements and stresses expression, the detail expressions of the relevant components in Eq. (12) can be written as (Yi et al., 2016):

(1) In intact rock mass:

$$\begin{cases} \sigma_{rr}^{(1)}=\frac{2\mu_1}{r^2}\sum_{n=0}^{\infty}\left(\varphi_0\varepsilon_n i^n\varepsilon_{11}^1+A_n\varepsilon_{11}^3+B_n\varepsilon_{12}^3\right)\cos n\theta \\ \sigma_{\theta\theta}^{(1)}=\frac{2\mu_1}{r^2}\sum_{n=0}^{\infty}\left(\varphi_0\varepsilon_n i^n\varepsilon_{21}^1+A_n\varepsilon_{21}^3+B_n\varepsilon_{22}^3\right)\cos n\theta \\ \sigma_{r\theta}^{(1)}=\frac{2\mu_1}{r^2}\sum_{n=0}^{\infty}\left(\varphi_0\varepsilon_n i^n\varepsilon_{41}^1+A_n\varepsilon_{41}^3+B_n\varepsilon_{42}^3\right)\sin n\theta \\ u_r^{(1)}=\frac{1}{r}\sum_{n=0}^{\infty}\left(\varphi_0\varepsilon_n i^n\varepsilon_{71}^1+A_n\varepsilon_{71}^3+B_n\varepsilon_{72}^3\right)\cos n\theta \\ u_\theta^{(1)}=\frac{1}{r}\sum_{n=0}^{\infty}\left(\varphi_0\varepsilon_n i^n\varepsilon_{81}^1+A_n\varepsilon_{81}^3+B_n\varepsilon_{82}^3\right)\sin n\theta \end{cases}. \tag{16}$$

(2) In EDZ:

$$\begin{cases} \sigma_{rr}^{(2)}=\frac{2\mu_2}{r^2}\sum_{n=0}^{\infty}\left(C_n\varepsilon_{11}^{31}+D_n\varepsilon_{11}^{41}+E_n\varepsilon_{11}^{32}+F_n\varepsilon_{11}^{42}+M_n\varepsilon_{12}^{32}+N_n\varepsilon_{12}^{42}\right)\cos n\theta \\ \sigma_{\theta\theta}^{(2)}=\frac{2\mu_2}{r^2}\sum_{n=0}^{\infty}\left(C_n\varepsilon_{21}^{31}+D_n\varepsilon_{21}^{41}+E_n\varepsilon_{21}^{32}+F_n\varepsilon_{21}^{42}+M_n\varepsilon_{22}^{32}+N_n\varepsilon_{22}^{42}\right)\cos n\theta \\ \sigma_{r\theta}^{(2)}=\frac{2\mu_2}{r^2}\sum_{n=0}^{\infty}\left(C_n\varepsilon_{41}^{31}+D_n\varepsilon_{41}^{41}+E_n\varepsilon_{41}^{32}+F_n\varepsilon_{41}^{42}+M_n\varepsilon_{42}^{32}+N_n\varepsilon_{42}^{42}\right)\sin n\theta \\ u_r^{(2)}=\frac{1}{r}\sum_{n=0}^{\infty}\left(C_n\varepsilon_{71}^{31}+D_n\varepsilon_{71}^{41}+E_n\varepsilon_{71}^{32}+F_n\varepsilon_{71}^{42}+M_n\varepsilon_{72}^{32}+N_n\varepsilon_{72}^{42}\right)\cos n\theta \\ u_\theta^{(2)}=\frac{1}{r}\sum_{n=0}^{\infty}\left(C_n\varepsilon_{81}^{31}+D_n\varepsilon_{81}^{41}+E_n\varepsilon_{81}^{32}+F_n\varepsilon_{81}^{42}+M_n\varepsilon_{82}^{32}+N_n\varepsilon_{82}^{42}\right)\sin n\theta \\ w_r=\frac{1}{r}\sum_{n=0}^{\infty}\left(\xi_1C_n\varepsilon_{71}^{31}+\xi_1D_n\varepsilon_{71}^{41}+\xi_2E_n\varepsilon_{71}^{32}+\xi_2F_n\varepsilon_{71}^{42}+\xi_sM_n\varepsilon_{72}^{32}+\xi_sN_n\varepsilon_{72}^{42}\right)\cos n\theta, \\ P_f=\sum_{n=0}^{\infty}\left(C_n\varepsilon_{91}^{31}+D_n\varepsilon_{91}^{41}+E_n\varepsilon_{91}^{32}+F_n\varepsilon_{91}^{42}\right)\cos n\theta \end{cases} \tag{17}$$

where $\varepsilon_{11}^{11},\cdots,\varepsilon_{ij}^{kl},\cdots,\varepsilon_{91}^{42}$ are the contribution of various waves for stresses and displacements (see Appendix A). We can obtain the values of A_n, B_n, $\cdots$, N_n by introducing Eq. (12) and Eq. (16) into Eq. (17) to solve the infinite system of linear equations:

$$\begin{bmatrix} -E_{71}^{3} & -E_{72}^{3} & E_{71}^{31} & E_{71}^{41} & E_{71}^{32} & E_{71}^{42} & E_{72}^{32} & E_{72}^{42} \\ -E_{81}^{3} & -E_{82}^{3} & E_{81}^{31} & E_{81}^{41} & E_{81}^{32} & E_{81}^{42} & E_{82}^{32} & E_{82}^{42} \\ -\widetilde{\mu}E_{11}^{3} & -\widetilde{\mu}E_{12}^{3} & E_{11}^{31}(r_1) & E_{11}^{41}(r_1) & E_{11}^{32}(r_1) & E_{11}^{42}(r_1) & E_{12}^{32}(r_1) & E_{12}^{42}(r_1) \\ -\widetilde{\mu}E_{41}^{3} & -\widetilde{\mu}E_{42}^{3} & E_{41}^{31}(r_1) & E_{41}^{41}(r_1) & E_{41}^{32}(r_1) & E_{41}^{42}(r_1) & E_{42}^{32}(r_1) & E_{42}^{42}(r_1) \\ 0 & 0 & E_{11}^{31}(r_2) & E_{11}^{41}(r_2) & E_{11}^{32}(r_2) & E_{11}^{42}(r_2) & E_{12}^{32}(r_2) & E_{12}^{42}(r_2) \\ 0 & 0 & E_{41}^{31}(r_2) & E_{41}^{41}(r_2) & E_{41}^{32}(r_2) & E_{41}^{42}(r_2) & E_{42}^{32}(r_2) & E_{42}^{42}(r_2) \\ 0 & 0 & \xi_1 E_{71}^{31}(r_1) & \xi_1 E_{71}^{41}(r_1) & \xi_2 E_{71}^{32}(r_1) & \xi_2 E_{71}^{42}(r_1) & \xi_s E_{72}^{32}(r_1) & \xi_s E_{72}^{42}(r_1) \\ 0 & 0 & E_{91}^{32}(r_2) & E_{91}^{42}(r_2) & E_{92}^{32}(r_2) & E_{92}^{42}(r_2) & 0 & 0 \end{bmatrix} \begin{bmatrix} A_n \\ B_n \\ C_n \\ D_n \\ E_n \\ F_n \\ M_n \\ N_n \end{bmatrix} = \varphi_0 \varepsilon_n \mathrm{i}^n \begin{bmatrix} E_{71}^{1} \\ E_{81}^{1} \\ \widetilde{\mu}E_{11}^{1} \\ \widetilde{\mu}E_{41}^{1} \\ 0 \\ 0 \\ 0 \\ 0 \end{bmatrix}, \tag{18}$$

where $E_{11}{}^{11},\cdots$, $E_{ij}{}^{kl},\cdots,E_{91}{}^{42}$ are the values of $\varepsilon_{11}{}^{11},\cdots$, $\varepsilon_{ij}{}^{kl},\cdots$, $\varepsilon_{91}{}^{42}$ in Appendix A when $r = r_1$ and $r = r_2$; $\widetilde{\mu}=\mu_1/\mu_2$.

The values of stress and displacement components can be obtained by introducing these unknown coefficients calculated in Eq. (18). Furthermore, the dynamic stress concentration factor (DSCF) is put forward to characterize the general law of varying stress around excavated tunnel (Tao et al., 2023b, 2020b), and the DSCF is defined as the ratio of the hoop stress around the tunnel to the stress amplitude when the incident wave propagated in the intact rock mass. The stress amplitude can be written in the following form of $\sigma_{\mathrm{m}} = \mu_1\varphi_0\beta$. Therefore, the DSCF expressions in the vicinity of the inner wall of the circular tunnel containing EDZ and the interface between the intact rock mass and the EDZ can be respectively expressed as:

$$\begin{aligned} \sigma_{\theta\theta 1}^{*} &= \left|\frac{\sigma_{\theta\theta}^{(1)}}{\sigma_{\mathrm{m}}}\right| \\ &= \frac{2}{\beta_1^2\varphi_0 r_1^2}\sum_{n=0}^{\infty}\left(\varphi_0\varepsilon_n\mathrm{i}^n\varepsilon_{21}^{1} + A_n\varepsilon_{21}^{3} + B_n\varepsilon_{22}^{3}\right)\cos n\theta, \end{aligned} \tag{19}$$

$$\begin{aligned} \sigma_{\theta\theta 2}^{*} &= \left|\frac{\sigma_{\theta\theta}^{(2)}}{\sigma_{\mathrm{m}}}\right| \\ &= \frac{2\mu_2}{\mu_1\beta^2\varphi_0 r_2^2}\sum_{n=0}^{\infty}\left(C_n\varepsilon_{21}^{31} + D_n\varepsilon_{21}^{41} + E_n\varepsilon_{21}^{32} + F_n\varepsilon_{21}^{42} + M_n\varepsilon_{22}^{32} + N_n\varepsilon_{22}^{42}\right)\cos n\theta. \end{aligned} \tag{20}$$

5 Numerical calculations and analysis

In this section, numerical results are obtained by inputting the physical and mechanical parameters in independently developed codes. The input parameter values for the intact rock mass are compiled in Tables 1 and 2 presenting the input parameter values used for the EDZ. First of all, in order to verify the validity of the analytical solutions, the limiting case for regarding the EDZ as an elastic lining in a circular tunnel is taken into account, i.e., set M, α, f, η, and $\rho_{\mathrm{f}} \to 0$ and $\widetilde{\mu} = 2.9$. The thickness of the EDZ is defined as a dimensionless parameter $N = r_1/r_2$ and the value of N is 1.1. In this case, when incident wave number $\alpha_1 = 0.2$ and 1, the angular distribution of the DSCF around the inner wall of the circular tunnel containing EDZ is plotted in Fig. 3(a). The variation of the DSCF with wave numbers around the inner wall of the circular tunnel containing EDZ and the interface of the intact rock mass and the EDZ are shown in Fig. 3(b). The classical solution is reproduced accurately in the above numerical results of the limit case (Mow & Pao, 1971). Additionally, it can be seen that good and stable results can be obtained when the truncation term equals to 9, and $n = 9$ is employed in the following calculation.

Furthermore, the dimensionless parameters N and $\widetilde{\mu}$ are used to characterize the range and damage degree of the EDZ in this study, and these parameters corresponded with buried depth and excavation mothed. The dynamic responses around a deep buried water-rich tunnel containing EDZ have been investigated according to different values of N and $\widetilde{\mu}$. Figures. 4 and 5 present the variation characteristics of the DSCF when $N = 1.1$ with different

Table 1
Input parameter values for the elastic medium.

Parameter 1	Intact rock mass (elastic medium)
v_1	0.25
ρ_1 (kg/m^3)	2700

Table 2
Input parameter values for the saturated porous elastic medium.

Parameter 2	EDZ (saturated porous elastic medium)
v_2	0.2
E_2 (Pa)	10×10^9
α	1
M (Pa)	6×10^9
η (Pa·s)	1×10^{-3}
k_{f} (kg/m^3)	1×10^{-8}
f	0.2
ρ_{f} (kg/m^3)	1000
ρ_{s} (kg/m^3)	2200

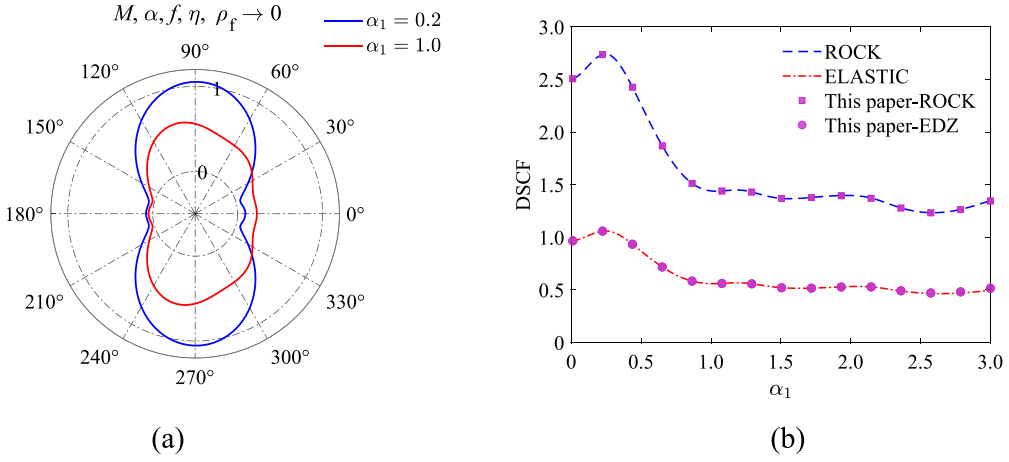

Fig.3. Distribution of the DSCF under different wave numbers and the variation of the DSCF with wave numbers. (a) Angular distribution, and (b) frequency distribution.

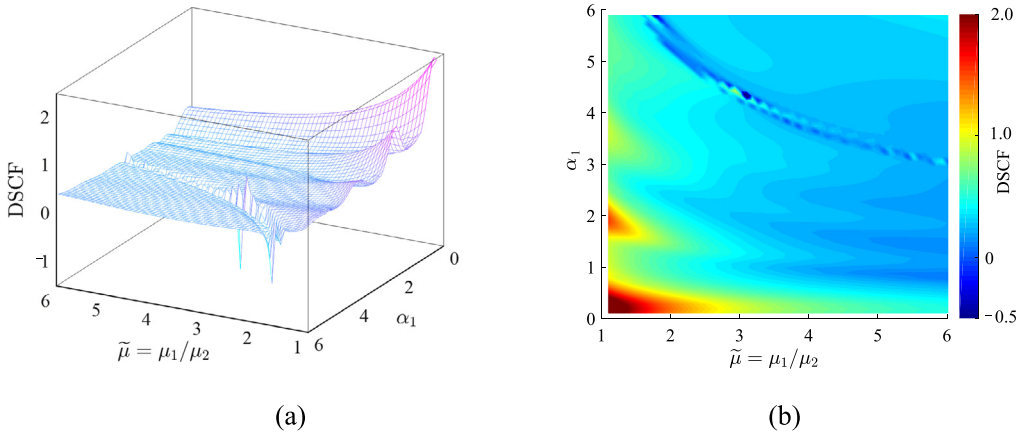

Fig. 4. Variation of DSCF at $\theta = 90°$ with different frequency P waves and damage degree under the thickness $N = 1.1$. (a) Three-dimensional contour map, and (b) thermodynamic map.

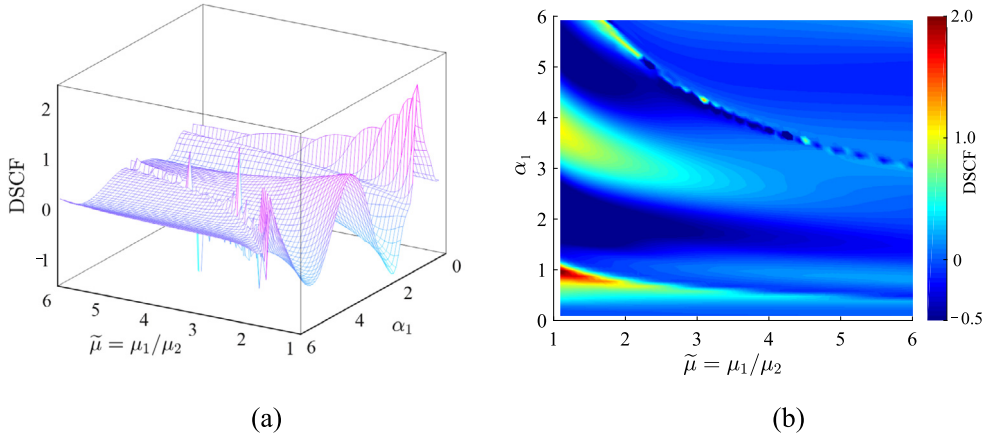

Fig. 5. Variation of DSCF at $\theta = 0°$ with different frequency P waves and damage degree under the thickness $N = 1.1$. (a) Three-dimensional contour map, and (b) thermodynamic map.

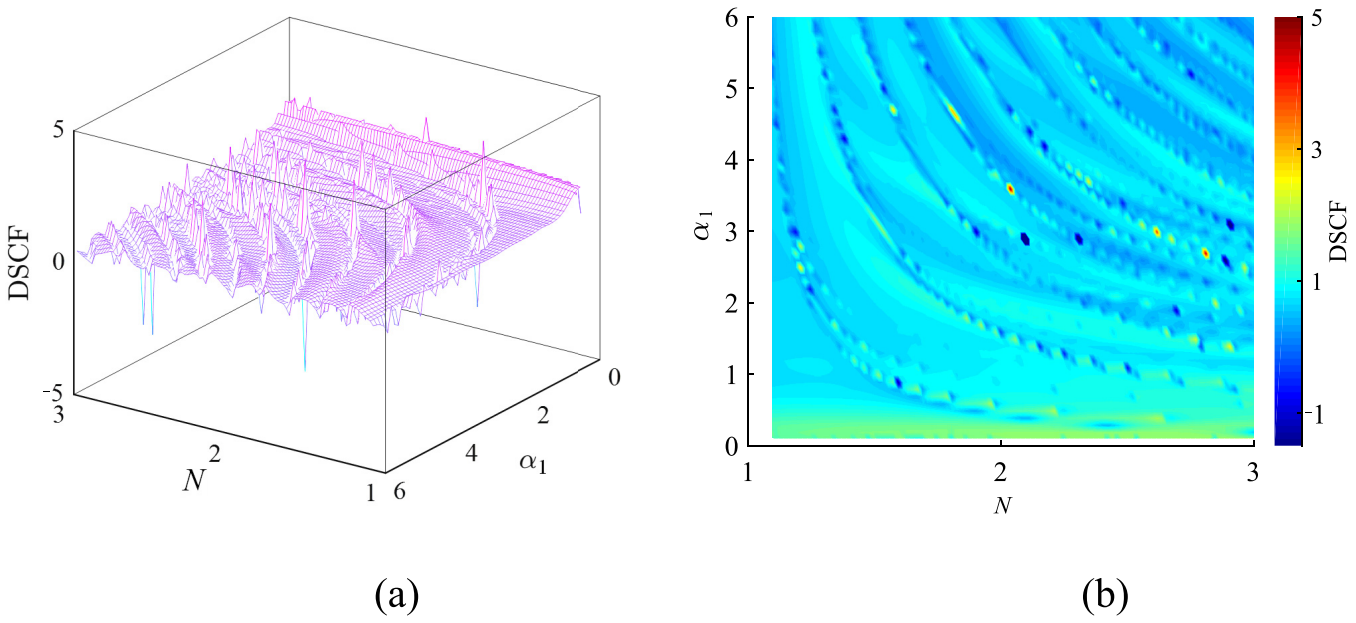

Fig. 6. Variation of DSCF at $\theta = 90°$ with different frequency P waves and thickness under the damage degree $\tilde{\mu} = 2$. (a) Three-dimensional contour map, and (b) thermodynamic map.

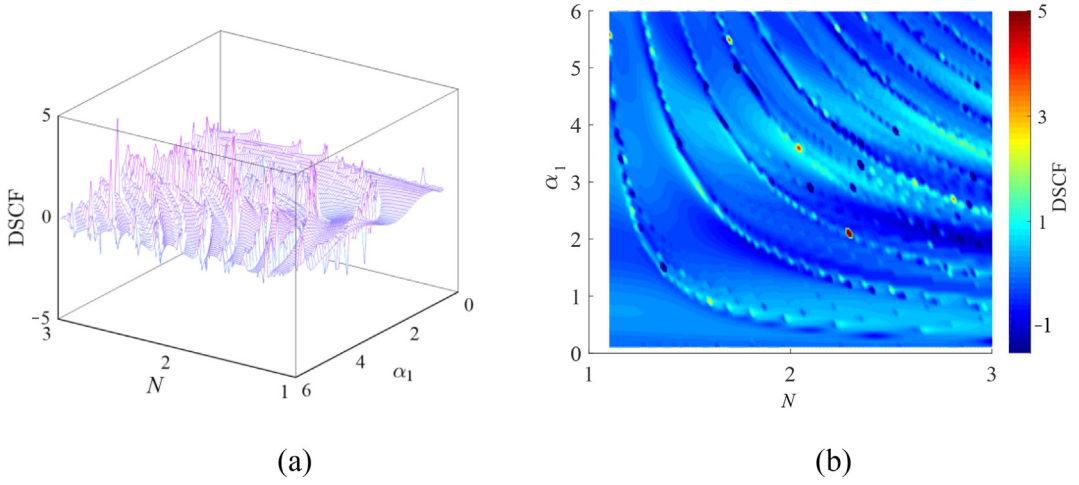

Fig. 7. Variation of DSCF at $\theta = 0°$ with different frequency P waves and thickness under the damage degree $\tilde{\mu} = 2$. (a) Three-dimensional contour map, and (b) thermodynamic map.

damage degrees under the action of different frequency P waves at $\theta = 90°$ and $\theta = 0°$, respectively. Overall, as the frequency and the damage degree parameter $\tilde{\mu}$ increased, the DSCF at $\theta = 90°$ and $\theta = 0°$ decreased gradually and tended to 0. The DSCF peaked at low frequency and low damage degree. When $\tilde{\mu}$ was not large, the DSCF oscillated with the increase of frequency, especially at $\theta = 0°$. As shown in Fig. 5, the DSCF increased quickly followed by a quick descent and negative values appeared that is alternated compression stress and tensile stress. A curve of intensive oscillation can be observed at $\alpha_1 > 3$, which seems important to be on guard against. Furthermore, EDZ around the deep buried water-rich tunnel induced by excavation can be considered as a flexible cushion, which can effectively reduce dynamic stress concentration around the tunnel subjected to the dynamic disturbance on the premise of not caving.

The variation of the DSCF at $\theta = 90°$ and $\theta = 0°$ with different frequencies and different thicknesses when $\tilde{\mu} = 2$ is shown in Figs. 6 and 7, respectively. It can be seen that the value of the DSCF is in the range of 0–1, and the DSCF is sensitive for changing in thickness parameters. Noting that the degree and the density of oscillations of the DSCF will increase with the increase of frequency and thickness. For

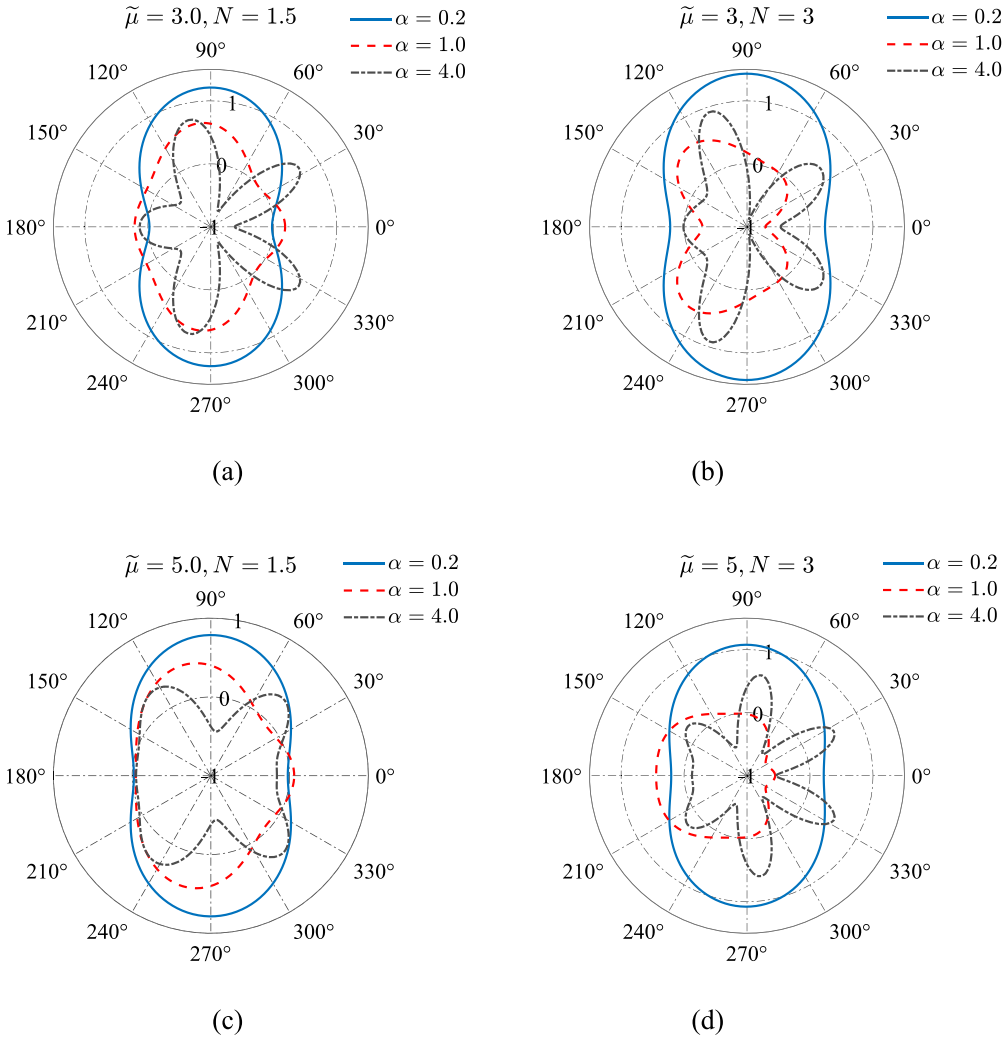

Fig. 8. Distribution of DSCF under different parameters subjected to different frequency P waves. (a) DSCF when $\widetilde{\mu} = 2.0$ and $N = 1.5$, (b) DSCF when $\widetilde{\mu} = 3$ and $N = 3$, (c) DSCF when $\widetilde{\mu} = 5.0$, $N = 1.5$, and (d) DSCF when $\widetilde{\mu} = 5$ and $N = 3$.

the position of $\theta = 90°$ shown in Fig. 6, the values of the DSCF are mainly 1 and the fluctuating range of the DSCF curve is smaller. As shown in Fig. 7, for the position of $\theta = 0°$, the DSCF values is mainly 0, and the oscillation amplitude is higher and more prone to tensile stress.

The angular distribution of the DSCF subjected to plane P wave is plotted in Fig. 8(a)–(d), corresponding to different parameters and frequencies. The curves of DSCF due to low frequency P wave appeared smoother than those due to high-frequency P wave and that has the minimum oscillation amplitude. The values at the propagation direction ($\theta = 0°$ or 180°) were close to 0 and those at perpendicular direction of propagation ($\theta = 90°$ or 270°) were close to 1 under the action of low frequency. There were multiple extreme values around the tunnel containing EDZ under the action of high frequency, which were the result of the scattering wave repeatedly propagated in the saturated porous elastic medium. In addition, the greater tensile stress concentration was observed on the illuminated side of the circular tunnel ($\theta = 0°$), whereas the same large tensile stress concentration was observed at perpendicular direction of propagation in the case of $\widetilde{\mu} = 3$, $N = 3$ and $\widetilde{\mu} = 5$, $N = 1.5$ as shown in Fig. 8(b) and (c).

6 Transient response and numerical example

In this section, we investigate the transient response surrounding a circular tunnel that contains EDZ in a water-rich environment. Specifically, we examine the influence of waveforms and incident wavelengths on the transient response. These investigations are particularly relevant as they simulate the effects of anharmonic disturbances commonly encountered in practical engineering scenarios. By analyzing the response of the tunnel system under different waveforms and incident wavelengths, we gain valuable insights into the dynamic behavior and potential risks associated with the EDZ in water-rich environments.

The introduction of Fourier transforms, the transient wave can be obtained by decomposing and then

superposing the harmonic wave with different frequencies. Hence, the transient response under an arbitrary excitation function $f(t)$ can be written as (Tao et al., 2020a):

$$u(x,t)=\frac{1}{\sqrt{2\pi}}\int_{-\infty}^{+\infty}\chi(x,\omega)F(\omega)\mathrm{e}^{-\mathrm{i}\omega t}\mathrm{d}\omega, \tag{21}$$

where $\chi(x,\omega)$ is the admittance function that is the real component of the steady state response of Eq. (19); $F(\omega)$ is the Fourier spectrum of the excitation function $f(t)$.

Taking the half-sine curve as the excitation function $f(t)$ to equivalent blast load, which can be written as (Tao et al., 2020a):

$$f(t)=\begin{cases}\sin(\frac{\pi t}{t_0}), 0\leqslant t<t_0\\ 0, \quad t\geqslant t_0\end{cases}, \tag{22}$$

where t_0 is the period of the waveform. In order to simplify the calculation, the dimensionless parameter $\bar{t}=c_{\mathrm{p}}t/r$ was used to indicate time travelling through the length of a radius, where c_{p} is the wave velocity of the incident P wave.

Meanwhile, the $\delta(t)$ function and Heaviside step function were introduced into Eq. (21), and according to the Duhamel integral, the transient DSCF can be obtained (Tao et al., 2020a):

$$\bar{\sigma}^{*}_{\theta\theta}=\begin{cases}\int_0^{\infty}\frac{\chi(x,\omega)}{\omega}\left[\frac{\cos\omega t-\cos(\pi t/t_0)}{\pi-\omega t_0}-\frac{\cos\omega t-\cos(\pi t/t_0)}{\pi+\omega t_0}\right]\mathrm{d}\omega, & 0\leqslant t<t_0\\ \int_0^{\infty}\frac{\chi(x,\omega)}{\omega}\left[\frac{\cos\omega t-\cos(\pi+\omega t-\omega t_0)}{\pi-\omega t_0}-\frac{\cos\omega t-\cos(\pi+\omega t_0-\omega t)}{\pi+\omega t_0}\right]\mathrm{d}\omega, & t\geqslant t_0\end{cases}. \tag{23}$$

The parameters $\tilde{\mu}=3$ and $N=3$ were used to calculate, the half-sine excitation function was controlled by the period t_0, so the characteristics of the transient response under different period could be investigated in this study.

As shown in Fig. 9(a) and (b), corresponding to $\theta=90°$ and $\theta=0°$, the transient DSCF increased rapidly to a positive peak value and decreased rapidly to negative values, and finally recovered to 0 gradually. This indicated that the process of decreasing from the compressive stress peaking to the generation of the tensile stress was experienced around the tunnel when the transient stress wave scattered on the periphery of the tunnel. The compressive stress concentration was greater than the tensile stress concentration at $\theta=90°$, and the longer the period t_0, the larger the tensile stress concentration and longer the time of recovering to 0. The oscillation after the transient DSCF recovered to 0 was observed in Fig. 9(a) and the complexity of oscillation was most when $t_0=5$. As shown in Fig. 9(b), at $\theta=0°$, the tensile stress concentration caused by transient stress wave was greater than the compressive stress concentration, and the amplitude of the oscillation in this position was greater than the position of $\theta=90°$. As the period t_0 increased, the dynamic stress concentration decreased. When $t_0=100$, with the increase of time, the stress state at the propagation direction of the tunnel with EDZ was always tensile stress concentration.

The distribution of the transient DSCF is plotted in Fig. 10 when $t_0=20$ and 100, and the region of the tunnel at perpendicular direction of propagation under the action of a transient stress wave displayed mainly compressive stress concentration. The peak value of compressive stress concentration was deviated to the shadow side ($\theta=180°$) at $\bar{t}=15$ and that to the illuminated side at $\bar{t}=20$. In addition, the possible tensile damage at the propagation direction must be alert. As shown in Fig. 10(b), the result investigated that the dynamic stress concentration was symmetrical distribution when incident period $t_0=100$. When the action time of stress wave increased to 100, the main stress state around the tunnel is tensile stress concentration.

The state of dynamic stress in the EDZ subjected to a transient half-sine wave when $t_0=20$ and 100 is shown in Fig. 11(a)–(f), respectively. For the tunnel roof and floor, the range of the compressive stress extended in arc shape

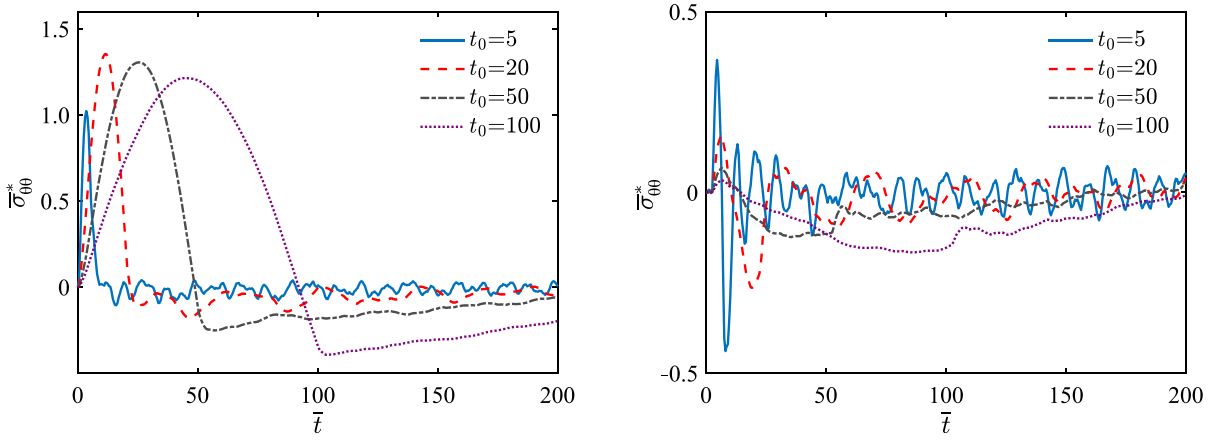

Fig. 9. Transient response under the action of the half-sine wave with different periods. (a) $\theta=90°$, and (b) $\theta=0°$.

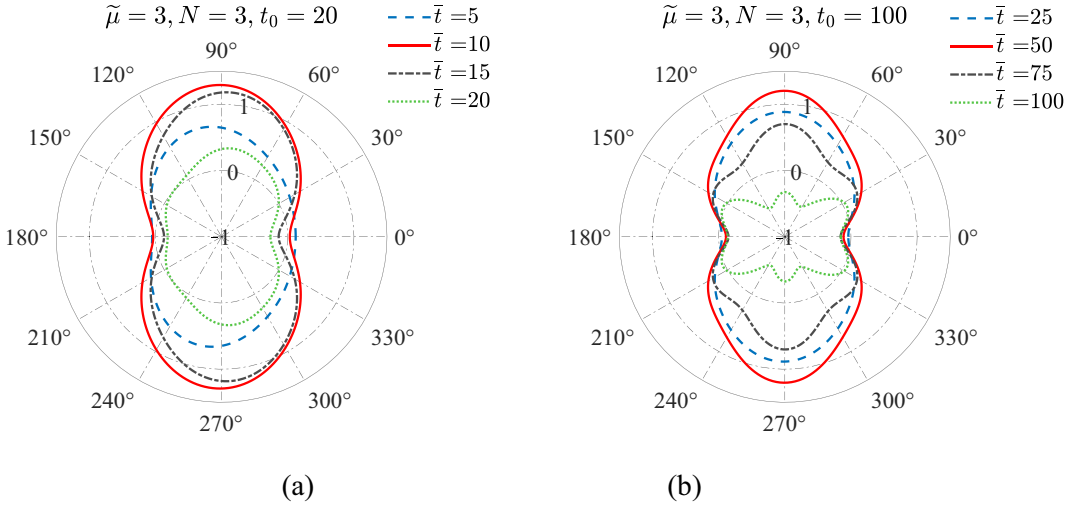

Fig. 10. Distribution of transient DSCF under the action of the transient wave with different periods. (a) $t_0 = 20$, and (b) $t_0 = 100$.

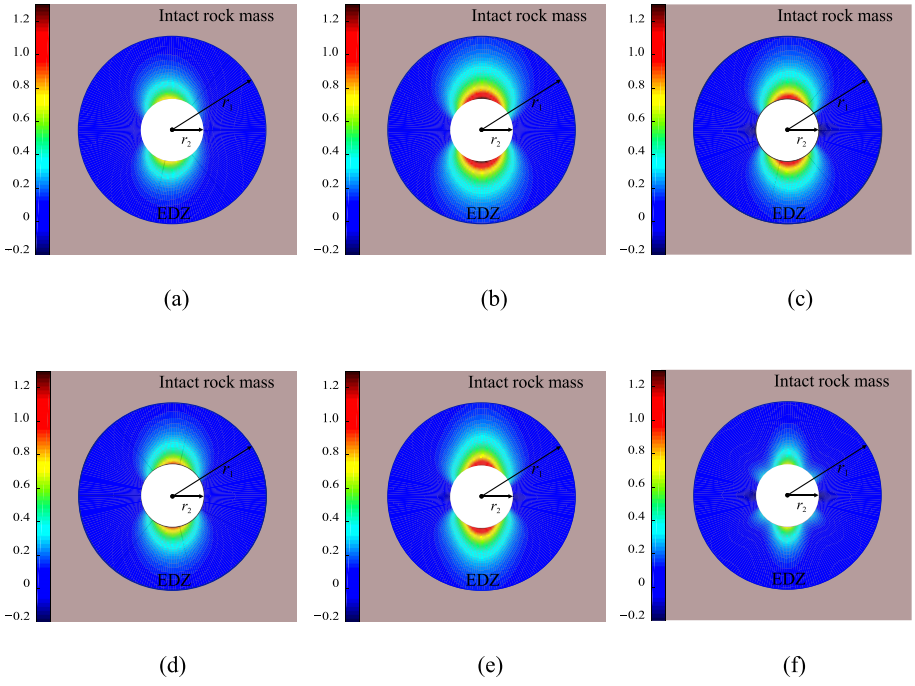

Fig. 11. Change process of dynamic stress in the EDZ under the action of the transient incident waves. (a)–(c) The wavelength $t_0 = 20$, and (d)–(f) the wavelength $t_0 = 100$.

from the inner wall of the roadway to the outside, and the peak value of compressive stress is displayed at the inner wall of the roadway. As the range of the stress and time increased, the value of stress peaked and decreased gradually. Furthermore, it should be noted that tensile stress has been observed on both sides of the tunnel as time progresses.

For simulating the explosive loads better, in addition to the half-sine wave mentioned above, the needle wave is also adopted commonly, which provide the following characteristic of rising quickly and descent slowly. The needle waveform can be written in the form (Tao et al., 2019):

$$f(t) = \begin{cases} e^{\frac{\alpha}{\beta}\arctan\left(\frac{\beta}{\alpha}\right)}\sqrt{1+\left(\frac{\alpha}{\beta}\right)^2}\cdot e^{-\alpha t}\cdot \sin\beta t, \ 0 \leqslant t < t_0 \\ 0\ , \ t \geqslant t_0 \end{cases}, \tag{24}$$

where t_0 is the period of the needle wave, the meaning of t is the same as $\bar{t}$ mentioned above, the parameters $\beta = \pi/t_0$, and $\alpha = \beta\cot(\beta t_1)$, where t_1 is the time of peak value. Furthermore, the term "ratio" as the ratio of the waveform peaking to the total time is defined to quantify the peak arrival time, where ratio $= t_1/t_0$.

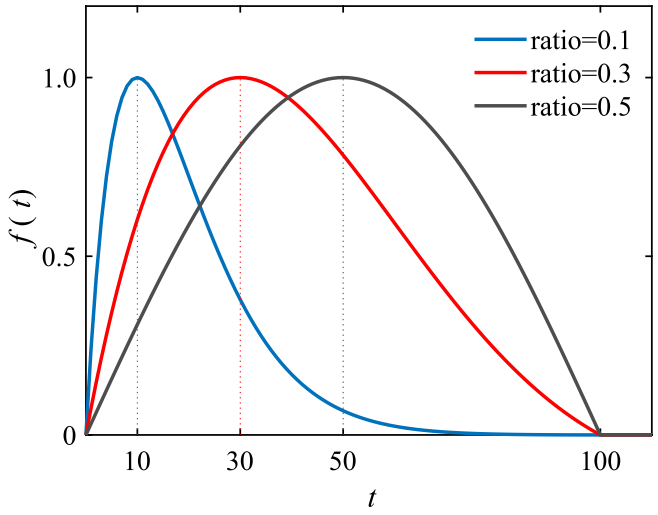

Fig. 12. Equivalent blasting curve with different "ratio" when $t_0 = 100$.

The transient waveform corresponding to different ratios when period $t_0 = 100$ is plotted in Fig. 12. The curve at ratio = 0.5 is the same as the waveform of the half-sine wave. The scale of the period t_0 can be considered as different wavelengths. Therefore, the transient response under different wavelengths and waveform ratios was investigated.

The transient response around the circular tunnel containing EDZ under the action of the equivalent blasting wave can be derived by using the same method as above, the expression is:

$$\bar{\sigma}^{*}_{\theta\theta} = \begin{cases} \frac{2}{\pi}\int_0^{\infty} \frac{\chi(x,\omega)}{\omega} \cdot [G(t)]\mathrm{d}\omega, & 0 \leqslant t < t_0 \\ \frac{2}{\pi}\int_0^{\infty} \frac{\chi(x,\omega)}{\omega} \cdot [G(t_0)]\mathrm{d}\omega, & t \geqslant t_0 \end{cases}, \tag{25}$$

where the $G(t)$ is an integral expression, which can be written as:

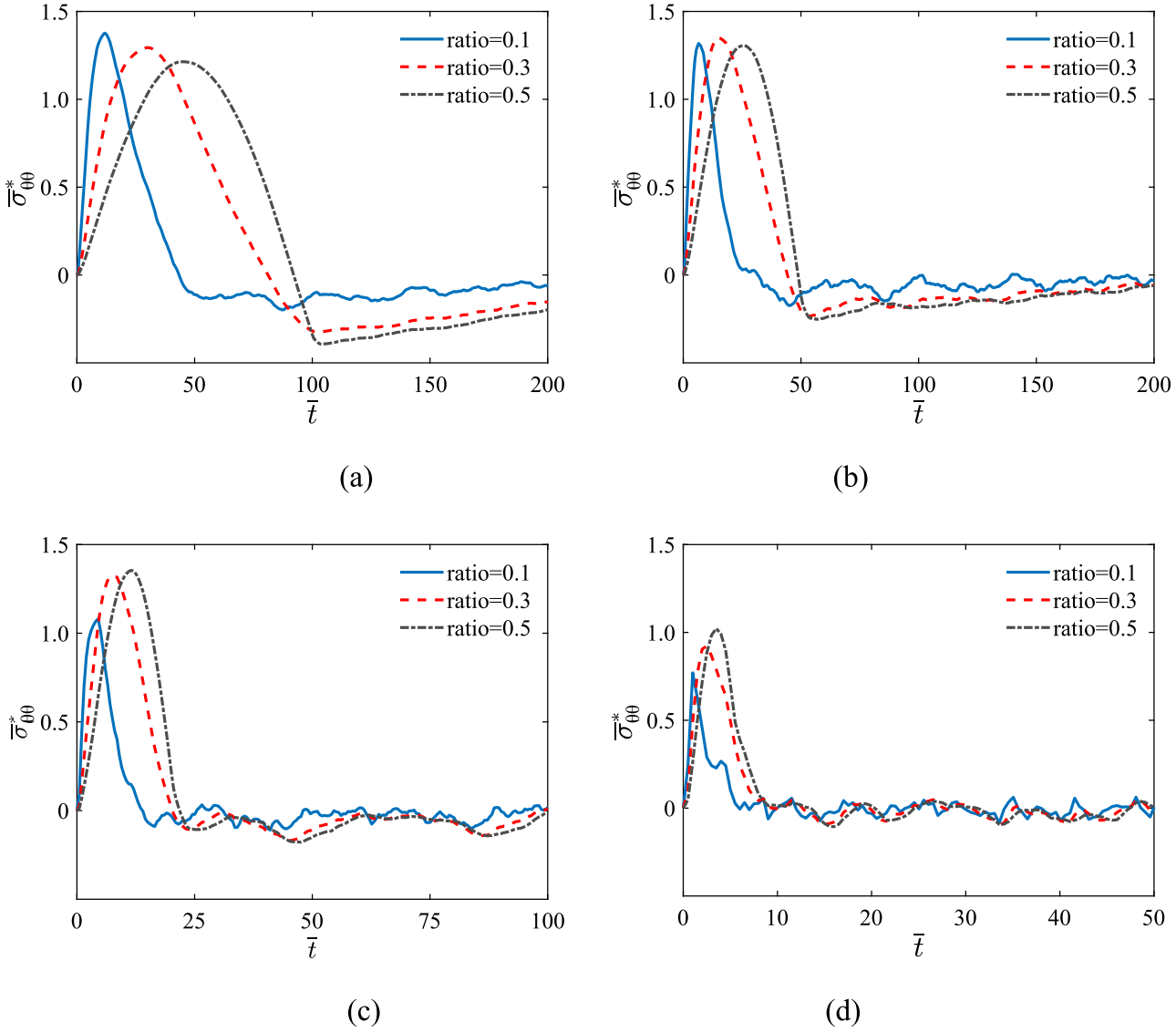

Fig. 13. Transient response under the action of the needle wave with different ratios and wavelengths at $\theta = 90°$. (a) $t_0 = 100$, (b) $t_0 = 50$, (c) $t_0 = 20$, and (d) $t_0 = 5$.

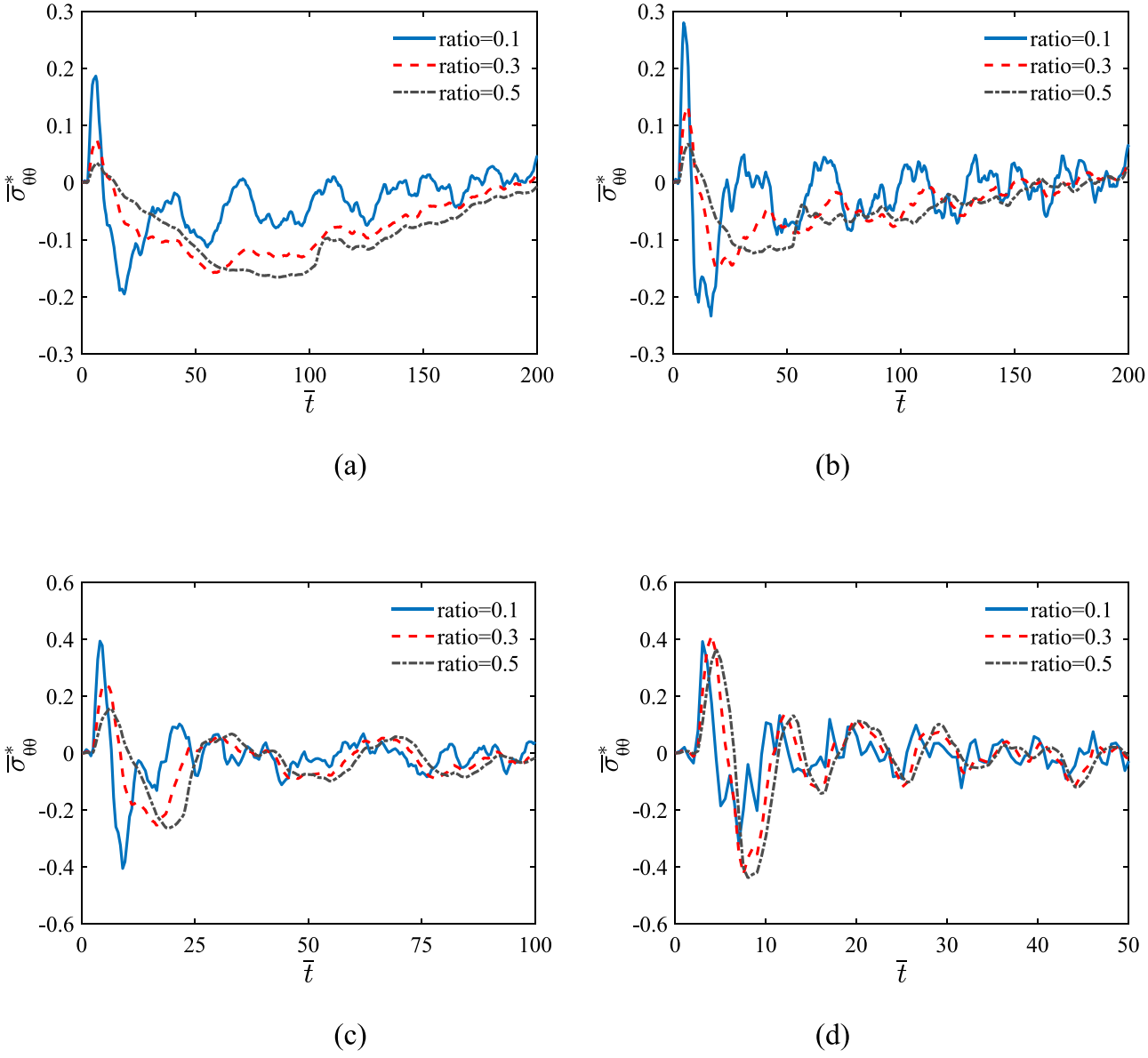

Fig. 14. Transient response under the action of the needle wave with different ratios and wavelengths at $\theta = 0°$. (a) $t_0 = 100$, (b) $t_0 = 50$, (c) $t_0 = 20$, and (d) $t_0 = 5$.

$$\begin{cases} G(t) = \int_0^t f'(\tau) \cdot \sin \omega(t-\tau)\ \mathrm{d}\tau,\ 0 \leqslant t < t_0 \\ G(t_0) = \int_0^{t_0} f'(\tau) \cdot \sin \omega(t-\tau)\ \mathrm{d}\tau,\ t \geqslant t_0 \end{cases} . \tag{26}$$

The same parameters of the EDZ and the intact rock mass as above are adopted into the calculation, and the numerical results are shown in Figs. 13 and 17. The variations of the transient DSCF with different ratios and wavelengths were plotted in Fig. 13(a)–(d) respectively. The transient response also oscillated during the process of recovering to 0 after arriving to negative peak value; the longer the wavelength, the greater the degree of the oscillation and the smaller the tensile stress. For different waveform ratios, firstly, the peak value of compressive stress decreased with the decrease of wavelength when ratio = 0.1. Secondly, when ratio = 0.3, there was the same peak value with different wavelengths except when $t_0 = 5$. Finally, the curves of the transient dynamic stress concentration subjected to the needle wave when ratio = 0.5 were found to be the same as that subjected to the half-sine wave. Overall, when the wavelength was longer, the compressive stress peak value occurred at the smaller value of the waveform ratio, and the transient DSCF was generally small when the wavelength was shorter.

The curve of transient DSCF at the position of $\theta = 0°$ is shown in Fig. 14(a)–(d), the transient DSCF varying violently at the illuminated side with the dimensionless time at different wavelengths and waveform ratios. For the longer wavelengths ($t_0 = 100$ and 50), the maximum ampli-

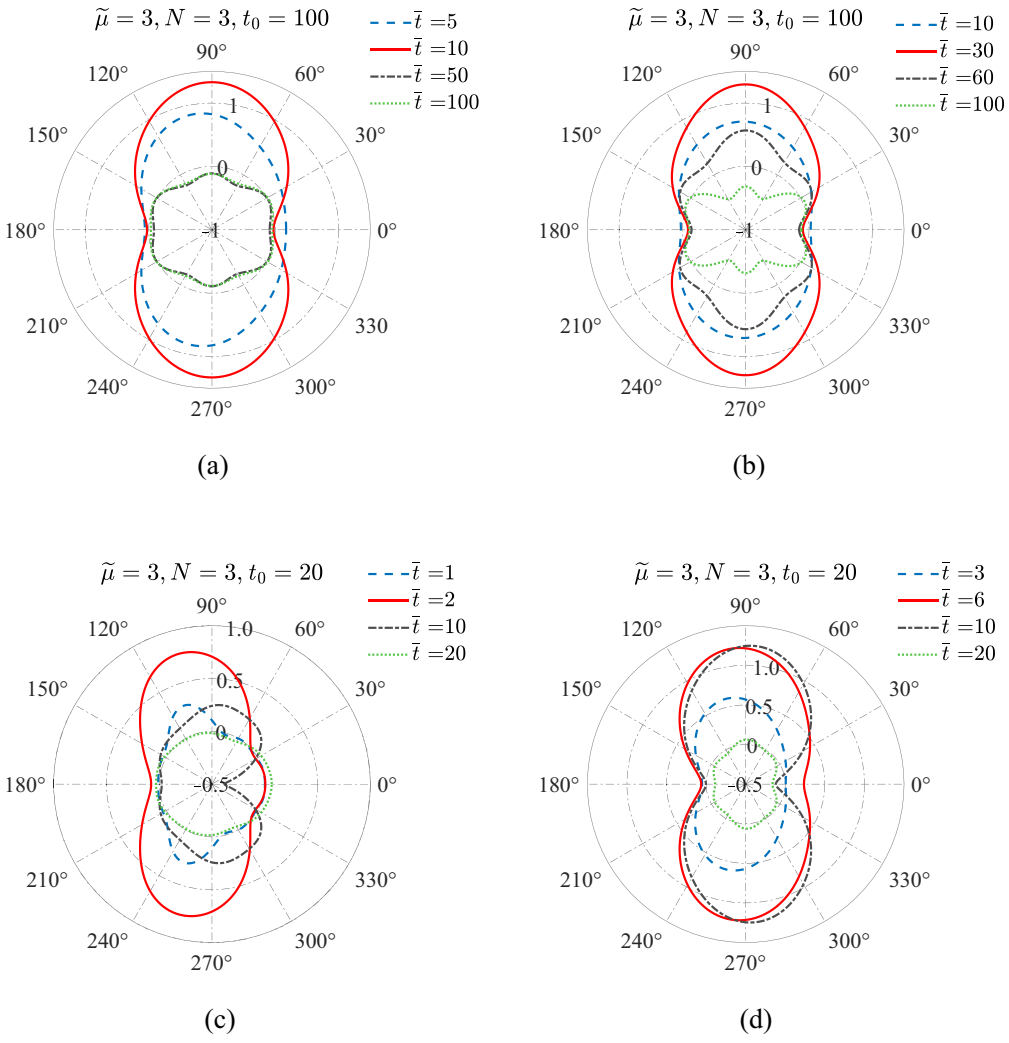

Fig. 15. Distribution of transient DSCF under the action of the transient needle wave with different wavelength and ratio. (a) ratio = 0.1, t_0 = 100, (b) ratio = 0.3, t_0 = 100, (c) ratio = 0.1, t_0 = 20, and (d) ratio = 0.3, t_0 = 20.

tude and degree of oscillation of transient DSCF occurred when the ratio equals to 0.1, and the transient DSCF at the illuminated side of the circular tunnel experienced the process of the compressive stress concentration peaked rapidly, then decreased to tensile stress peak value, next recovered to 0 and oscillated near 0 in the end. In addition, noting the tunnel was mainly under the state of tensile stress at this position when ratio = 0.3 and 0.5. The peak values of compressive stress and tensile stress caused by stress wave with a wavelength less than 20 were greater than that when the wavelength was longer. Moreover, the trend of transient DSCF varying at different waveform ratios was similar to each other when t_0 = 5.

From Fig. 15(a)–(d), we can see that the characteristic of the distribution of transient DSCF around the circular tunnel caused by needle stress wave when t_0 = 100 and ratio = 0.3 is similar to the half-sine wave. The transient DSCF distributed around the tunnel symmetrically under the longer wavelength incident wave, only that the deviation will take place to one side at t = 5 when ratio = 0.1 (see Fig. 15(a)). The angular distribution of transient DSCF around the tunnel under the action of the smaller wavelength incident wave was plotted in Fig. 15(c) and (d). The result shows that the fluctuation degree of the distribution of stress is greater under short wavelength than that under long wavelength. Especially the tensile stress concentration is at the illuminated side after peaking.

The process of stress transfer in the EDZ is shown in Fig. 16(a)–(f) and Fig. 17 (a)–(f) subjected to different wavelength needle waves in order to better understand the stress state around the tunnel containing EDZ. For the case of long wavelength incidence, see Fig. 16, there was a trend of the region of compressive stress offset to the shadow side at first due to the scattering of stress wave around the tunnel. Subsequently, the region extended in arc shape from the inner wall of the roadway to the outside and recovered to symmetric distribution, which the process was the same as the half-sine wave incidence. Near the end of time of stress wave travelling through the tunnel, the tensile stress concentration was occurred at the tunnel roof

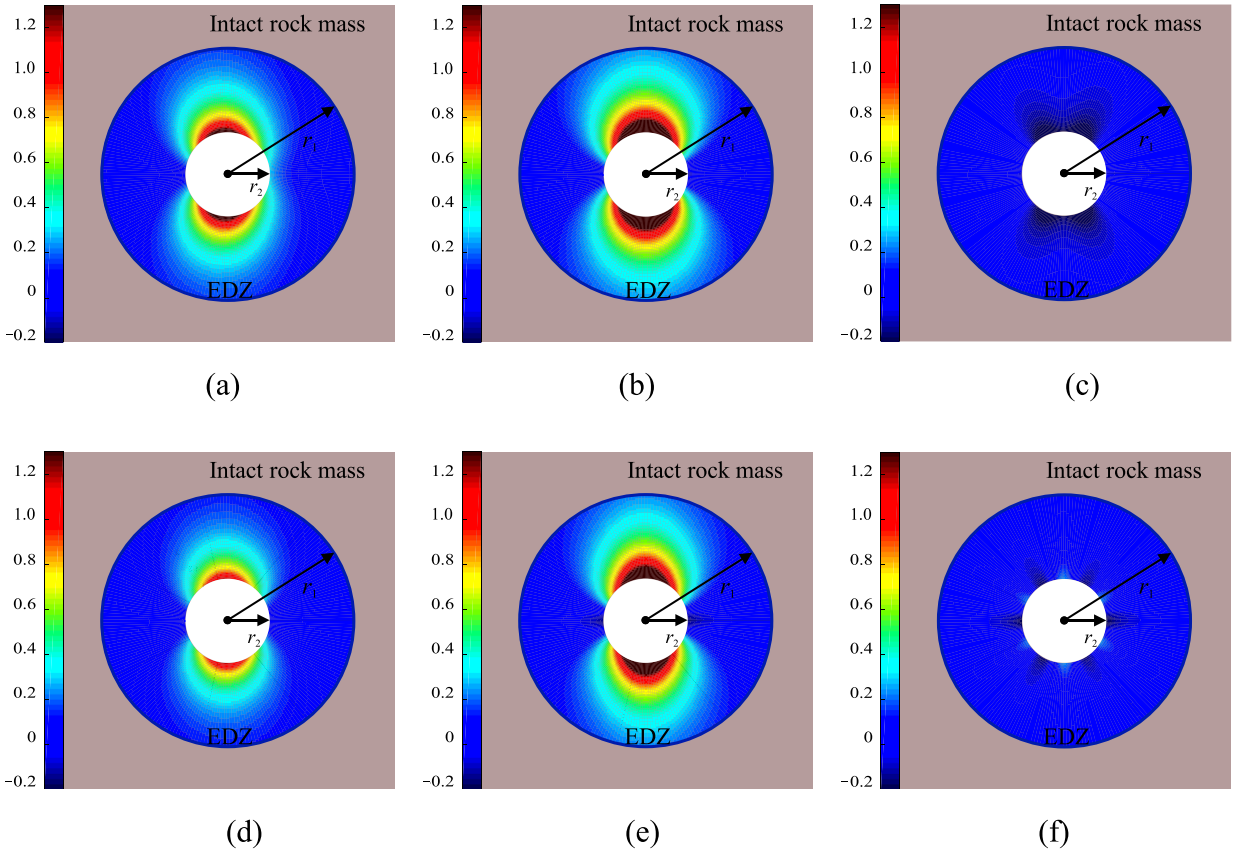

Fig. 16. Process of stress transfer in the EDZ under the action of the needle transient incident waves at wavelength $t_0 = 100$. (a)–(c) The waveform ratio = 0.1, and (d)–(f) the waveform ratio = 0.3.

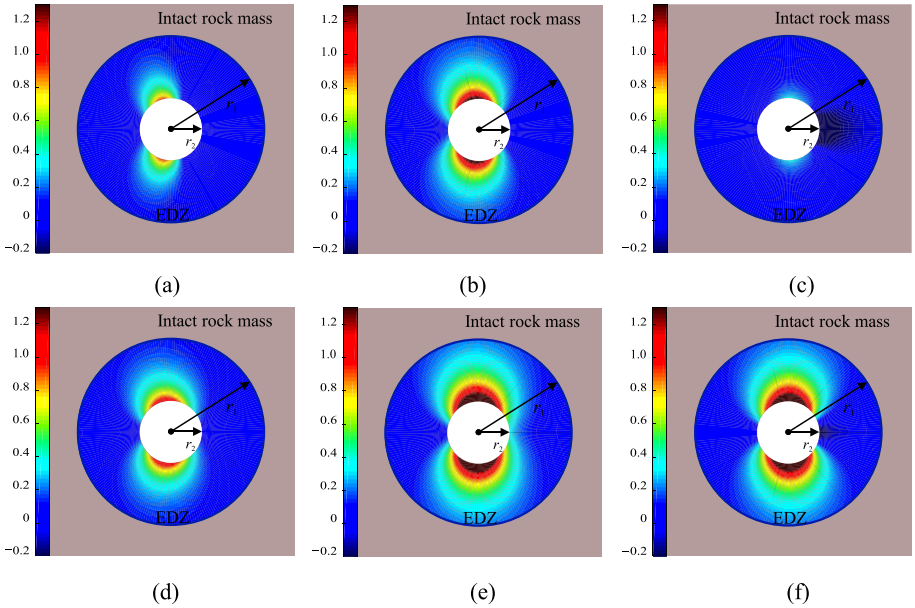

Fig. 17. Process of stress transfer in the EDZ under the action of the needle transient incident waves at wavelength $t_0 = 20$. (a)–(c) The waveform ratio = 0.1, and (d)–(f) the waveform ratio = 0.3.

and floor when the waveform ratio = 0.1, and that was occurred around the tunnel when the waveform ratio = 0.3 (see Fig. 16(c) and (f)). Meanwhile, noting that the tensile stress was already occurred at the both side of the tunnel when the waveform the ratio = 0.3 and peaking. The differences of stress state in the EDZ between the long wavelength incidence and the short wavelength incidence can be observed from Figs. 16 and 17, when the wavelength $t_0 = 20$, the offset degree of the region of compressive stress concentration was greater than that the case of long wavelength incidence. In the case of the short wavelength, stress wave scattered on the periphery of the tunnel containing EDZ, before the waveform arrived peak value, and the compressive stress concentration mainly occurred at the shadow side of the tunnel. Moreover, the tensile failure at the illuminated side needs to be alert near the end of time of short wavelength stress wave travelling through the tunnel.

Although the dynamic response of DSCF around a circular water-rich tunnel containing EDZ is clarified, there are still some restrictions that must to be noted. Firstly, the tunnel is set in a circular shape and the stress state within it is assumed to be a hydrostatic stress field and the intact rock mass outside is set as an elastic medium for analysis purposes. Secondly, the analytical solution is obtained by using wave function expansion method, it is important to note that the in-situ stress is not considered throughout the entire derivation process. In other words, the theoretical model is analyzed by separating the dynamic and static stress components. Finally, one of the assumptions made in the condition boundary is that the interface between the EDZ and the intact rock mass outside is perfect, which simplifies the analysis. On the other hand, for clarity, in the present article we consider a partially sealed boundary condition at the interface between the EDZ and the intact rock mass outside. Additionally, a permeable boundary condition is set at the inner wall of the tunnel. It should be noted that these assumptions may not fully capture the complexities and variations encountered in practical engineering scenarios.

7 Conclusions

The analytical solution of dynamic response around a circular water-rich tunnel containing the EDZ subjected to a plane P wave based on wave function expansion method and Fourier transform has been derived in this study. Biot's model of the saturated porous elastic medium is introduced to describe the EDZ and the dimensionless parameter variable $\widetilde{\mu}$ is defined to characterize the damage degree of the EDZ and buried depth of the tunnel. Some finding conclusions are obtained as follows:

(1) The dynamic stress became concentrated around EDZ subjected to P wave and induced strong vibrations as the frequencies increased and the variables changed. The sensitivity of DSCF to parameter N is greater than that to $\widetilde{\mu}$. Furthermore, the EDZ around the deep buried tunnel can be equaled a flexible cushion, which can reduce the stress concentration around the tunnel.
(2) Under the action of the transient incident wave which the excitation function was a half-sine waveform and needle waveform, the process of compressive stress concentration from rising to peak value and then decreasing to tensile stress concentration was experienced around the tunnel, it was mainly tensile stress concentration at the propagation direction, especially the maximum tensile stress appeared in the case of the short-wavelength incidence.
(3) The transient DSCF was mainly symmetrical distribution around the tunnel, and as time increased, the compressive stress at the perpendicular direction of propagation were extended to the depth in arc shape and reduced gradually. In addition, it was important to alert the possibility of the tensile damage at the tunnel roof and floor under the action of the long-wavelength needle wave. This study provides a reference for the support and the construction design of the tunnel containing EDZ in a water-rich environment.

Declaration of competing interest

The authors declare that they have no known competing financial interests or personal relationships that could have appeared to influence the work reported in this paper.

Acknowledgment

The research presented in this paper was supported by the National Natural Science Foundation of China (Grant Nos. 12072376 and 52274105).

Appendix A

$$E_{11}^{1} = \left[n^2 + n - \frac{1}{2}\beta_1^2 r_1^2\right] J_n(\alpha_1 r_1) - \alpha_1 r_1 J_{n-1}(\alpha_1 r_1) \tag{A1}$$

$$E_{11}^{3} = \left[n^2 + n - \frac{1}{2}\beta_1^2 r_1^2\right] H_n^{(1)}(\alpha_1 r_1) - \alpha_1 r_1 H_n^{(1)}(\alpha_1 r_1) \tag{A2}$$

$$E_{12}^{3} = n\left[-(n+1)H_n^{(1)}(\beta_1 r_1) + \beta_1 r_1 H_{n-1}^{(1)}(\beta_1 r_1)\right] \tag{A3}$$

$$E_{11}^{31} = \left[n^2 + n - \left(1 + \frac{\lambda_c + \alpha M \xi_1}{2\mu_2}\right)\alpha_{21}^2 r^2\right] H_n^{(1)}(\alpha_{21} r) - \alpha_{21} r H_{n-1}^{(1)}(\alpha_{21} r) \tag{A4}$$

$$E_{11}^{41} = \left[n^2 + n - \left(1 + \frac{\lambda_c + \alpha M \xi_1}{2\mu_2}\right)\alpha_{21}^2 r^2\right] H_n^{(2)}(\alpha_{21} r) - \alpha_{21} r H_{n-1}^{(2)}(\alpha_{21} r) \tag{A5}$$

$$E_{11}^{32}=\left[n^2+n-\left(1+\frac{\lambda_c+\alpha M\xi_2}{2\mu_2}\right)\alpha_{22}^2r^2\right]H_n^{(1)}(\alpha_{22}r)-\alpha_{22}rH_{n-1}^{(1)}(\alpha_{22}r) \tag{A6}$$

$$E_{11}^{42}=\left[n^2+n-\left(1+\frac{\lambda_c+\alpha M\xi_2}{2\mu_2}\right)\alpha_{22}^2r^2\right]H_n^{(2)}(\alpha_{22}r)-\alpha_{22}rH_{n-1}^{(2)}(\alpha_{22}r) \tag{A7}$$

$$E_{12}^{32}=n\left[-(n+1)H_n^{(1)}(\beta_2r)+\beta_2rH_{n-1}^{(1)}(\beta_2r)\right] \tag{A8}$$

$$E_{12}^{42}=n\left[-(n+1)H_n^{(2)}(\beta_2r)+\beta_2rH_{n-1}^{(2)}(\beta_2r)\right] \tag{A9}$$

$$E_{41}^{1}=-n[-(n+1)J_n(\alpha_1r)+\alpha_1rJ_{n-1}(\alpha_1r)] \tag{A10}$$

$$E_{41}^{3}=-n\left[-(n+1)H_n^{(1)}(\alpha_1r)+\alpha_1rH_{n-1}^{(1)}(\alpha_1r)\right] \tag{A11}$$

$$E_{42}^{3}=-\left(n^2+n-\frac{\beta_1^2r^2}{2}\right)H_n^{(1)}(\beta_1r)+\beta_1rH_{n-1}^{(1)}(\beta_1r) \tag{A12}$$

$$E_{41}^{31}=-n\left[-(n+1)H_n^{(1)}(\alpha_{21}r)+\alpha_{21}rH_{n-1}^{(1)}(\alpha_{21}r)\right] \tag{A13}$$

$$E_{41}^{41}=-n\left[-(n+1)H_n^{(2)}(\alpha_{21}r)+\alpha_{21}rH_{n-1}^{(2)}(\alpha_{21}r)\right] \tag{A14}$$

$$E_{41}^{32}=-n\left[-(n+1)H_n^{(1)}(\alpha_{22}r)+\alpha_{22}rH_{n-1}^{(1)}(\alpha_{22}r)\right] \tag{A15}$$

$$E_{41}^{42}=-n\left[-(n+1)H_n^{(2)}(\alpha_{22}r)+\alpha_{22}rH_{n-1}^{(2)}(\alpha_{22}r)\right] \tag{A16}$$

$$E_{42}^{32}=-\left(n^2+n-\frac{\beta_2^2r^2}{2}\right)H_n^{(1)}(\beta_2r)+\beta_2rH_{n-1}^{(1)}(\beta_2r) \tag{A17}$$

$$E_{42}^{42}=-\left(n^2+n-\frac{\beta_2^2r^2}{2}\right)H_n^{(2)}(\beta_2r)+\beta_2rH_{n-1}^{(2)}(\beta_2r) \tag{A18}$$

$$E_{71}^{1}=\alpha_1rJ_{n-1}(\alpha r)-nJ_n(\alpha_1r) \tag{A19}$$

$$E_{71}^{3}=\alpha_1rH_{n-1}^{(1)}(\alpha_1r)-nH_n^{(1)}(\alpha_1r) \tag{A20}$$

$$E_{72}^{3}=nH_n^{(1)}(\beta_1r) \tag{A21}$$

$$E_{71}^{31}=\alpha_1rH_{n-1}^{(1)}(\alpha_{21}r)-nH_n^{(1)}(\alpha_{21}r) \tag{A22}$$

$$E_{71}^{41}=\alpha_1rH_{n-1}^{(2)}(\alpha_{21}r)-nH_n^{(2)}(\alpha_{21}r) \tag{A23}$$

$$E_{71}^{32}=\alpha_{22}rH_{n-1}^{(1)}(\alpha_{22}r)-nH_n^{(1)}(\alpha_{22}r) \tag{A24}$$

$$E_{71}^{42}=\alpha_{22}rH_{n-1}^{(2)}(\alpha_{22}r)-nH_n^{(2)}(\alpha_{22}r) \tag{A25}$$

$$E_{72}^{32}=nH_n^{(1)}(\beta_2r) \tag{A26}$$

$$E_{72}^{42}=nH_n^{(2)}(\beta_2r) \tag{A27}$$

$$E_{81}^{1}=-nJ_n(\alpha_1r) \tag{A28}$$

$$E_{81}^{3}=-nH_n^{(1)}(\alpha_1r) \tag{A29}$$

$$E_{82}^{3}=-\left[\beta_1rH_{n-1}^{(1)}(\beta_1r)-nH_n^{(1)}(\beta_1r)\right] \tag{A30}$$

$$E_{81}^{31}=-nH_n^{(1)}(\alpha_{21}r) \tag{A31}$$

$$E_{81}^{41}=-nH_n^{(2)}(\alpha_{21}r) \tag{A32}$$

$$E_{81}^{32}=-nH_n^{(1)}(\alpha_{22}r) \tag{A33}$$

$$E_{81}^{42}=-nH_n^{(2)}(\alpha_{22}r) \tag{A34}$$

$$E_{82}^{32}=-\left[\beta_2rH_{n-1}^{(1)}(\beta_2r)-nH_n^{(1)}(\beta_2r)\right] \tag{A35}$$

$$E_{82}^{42}=-\left[\beta_2rH_{n-1}^{(2)}(\beta_2r)-nH_n^{(2)}(\beta_2r)\right] \tag{A36}$$

$$E_{91}^{32}=(\alpha+\xi_1)M\alpha_{21}^2H_n^{(1)}(\alpha_{21}r) \tag{A37}$$

$$E_{91}^{42}=(\alpha+\xi_1)M\alpha_{21}^2H_n^{(2)}(\alpha_{21}r) \tag{A38}$$

$$E_{92}^{32}=(\alpha+\xi_2)M\alpha_{22}^2H_n^{(1)}(\alpha_{22}r) \tag{A39}$$

$$E_{92}^{42}=(\alpha+\xi_2)M\alpha_{22}^2H_n^{(2)}(\alpha_{22}r) \tag{A40}$$

$$E_{21}^{31}=-\left[n^2+n+(\lambda_c+\alpha M\xi_1)/(2\mu_2)\alpha_{21}^2r^2\right]H_n^{(1)}(\alpha_{21}r)+\alpha_{21}rH_{n-1}^{(1)}(\alpha_{21}r) \tag{A41}$$

$$E_{21}^{41}=-\left[n^2+n+(\lambda_c+\alpha M\xi_1)/(2\mu_2)\alpha_{21}^2r^2\right]H_n^{(2)}(\alpha_{21}r)+\alpha_{21}rH_{n-1}^{(2)}(\alpha_{21}r) \tag{A42}$$

$$E_{21}^{32}=-\left[n^2+n+(\lambda_c+\alpha M\xi_2)/(2\mu_2)\alpha_{22}^2r^2\right]H_n^{(1)}(\alpha_{22}r)+\alpha_{22}rH_{n-1}^{(1)}(\alpha_{22}r) \tag{A43}$$

$$E_{21}^{42}=-\left[n^2+n+(\lambda_c+\alpha M\xi_2)/(2\mu_2)\alpha_{22}^2r^2\right]H_n^{(2)}(\alpha_{22}r)+\alpha_{22}rH_{n-1}^{(2)}(\alpha_{22}r) \tag{A44}$$

$$E_{22}^{32}=n\left[(n+1)H_n^{(1)}(\beta_2r)-\beta_2rH_{n-1}^{(1)}(\beta_2r)\right] \tag{A45}$$

$$E_{22}^{42}=n\left[(n+1)H_n^{(2)}(\beta_2r)-\beta_2rH_{n-1}^{(2)}(\beta_2r)\right] \tag{A46}$$

References

Biot, M. A. (1956a). Theory of propagation of elastic waves in a fluid-saturated porous solid. I. low-frequency range. *The Journal of the Acoustical Society of America, 28*(2), 168–178.

Biot, M. A. (1956b). Theory of propagation of elastic waves in a fluid-saturated porous solid. II. higher frequency range. *The Journal of the Acoustical Society of America, 28*(2), 179–191.

Bobet, A. (2009). Elastic solution for deep tunnels. Application to excavation damage zone and rockbolt support. *Rock Mechanics and Rock Engineering, 42*(2), 147–174.

Brown, E. (1980). *Underground excavations in rock*. CRC Press.

Brown, E. T., Bray, J. W., Ladanyi, B., & Hoek, E. (1983). Ground response curves for rock tunnels. *Journal of Geotechnical Engineering, 109*(1), 15–39.

Cho, W. J., Kim, J. S., Lee, C., & Choi, H.-J. (2013). Gas permeability in the excavation damaged zone at KURT. *Engineering Geology, 164*, 222–229.

Feng, X. T., Guo, H. S., Yang, C.-X., & Li, S.-J. (2018). In situ observation and evaluation of zonal disintegration affected by existing fractures in deep hard rock tunneling. *Engineering Geology, 242*, 1–11.

Gu, H. L., Lai, X. P., Tao, M., Cao, W. Z., & Yang, Z. K. (2023). The role of porosity in the dynamic disturbance resistance of water-saturated coal. *International Journal of Rock Mechanics and Mining Sciences, 166*, 105388.

Hasheminejad, S. M., & Avazmohammadi, R. (2007). Harmonic wave diffraction by two circular cavities in a poroelastic formation. *Soil Dynamics and Earthquake Engineering, 27*, 29–41.

Hasheminejad, S. M., & Hosseini, H. (2002). Radiation loading of a cylindrical source in a fluid-filled cylindrical cavity embedded within a fluid-saturated poroelastic medium. *Journal of Applied Mechanics, 69*(5), 675–683.

Jiang, L. F., Zhou, X. L., & Wang, J. H. (2009). Scattering of a plane wave by a lined cylindrical cavity in a poroelastic half-plane. *Computers and Geotechnics, 36*, 773–786.

Kaiser, P., Yazici, S., & Maloney, S. (2001). Mining-induced stress change and consequences of stress path on excavation stability—a case study. *International Journal of Rock Mechanics and Mining Sciences, 38*(2), 167–180.

Lai, J., Wang, Y. C., & Liu, Y. (2021). Blasting excavation induced damage caused to the rock mass surrounding tunnels. *IOP Conference Series: Earth and Environmental Science, 814*(1), 012013.

Li, W. H., Zhu, S. N., Lee, V. W., Shi, P. X., & Zhao, C. G. (2022). Scattering of plane SV-waves by a circular lined tunnel in an undersea saturated half-space. *Soil Dynamics and Earthquake Engineering, 153*, 107064.

Li, X. B., Cao, W. Z., Zhou, Z. L., & Zou, Y. (2014). Influence of stress path on excavation unloading response. *Tunnelling and Underground Space Technology, 42*, 237–246.

Li, X. B., Li, C. J., Cao, W. Z., & Tao, M. (2018). Dynamic stress concentration and energy evolution of deep-buried tunnels under blasting loads. *International Journal of Rock Mechanics and Mining Sciences, 104*, 131–146.

Li, X. B., & Weng, L. (2016). Numerical investigation on fracturing behaviors of deep-buried opening under dynamic disturbance. *Tunnelling and Underground Space Technology, 54*, 61–72.

Luo, S., Gong, F. Q., Peng, K., & Liu, Z. X. (2023). Influence of water on rockburst proneness of sandstone: Insights from relative and absolute energy storage. *Engineering Geology, 323*, 107172.

Martino, J. B., & Chandler, N. A. (2004). Excavation-induced damage studies at the underground research laboratory. *International Journal of Rock Mechanics and Mining Sciences, 41*(8), 1413–1426.

Mitaim, S., & Detournay, E. (2004). Damage around a cylindrical opening in a brittle rock mass. *International Journal of Rock Mechanics and Mining Sciences, 41*(8), 1447–1457.

Mow, C. C., & Pao, Y. H. (1971). *The diffraction of elastic waves and dynamic stress concentrations*. Santa Monica, CA: RAND Corporation.

Pao, Y. H., Mow, C. C., & Achenbach, J. D. (1973). Diffraction of elastic waves and dynamic stress concentrations. *Journal of Applied Mechanics, 40*(4), 872.

Read, R. S. (2004). 20 years of excavation response studies at AECL's underground research laboratory. *International Journal of Rock Mechanics and Mining Sciences, 41*(8), 1251–1275.

Senjuntichai, T., & Rajapakse, R. (1993). Transient response of a circular cavity in a poroelastic medium. *International Journal for Numerical and Analytical Methods in Geomechanics, 17*(6), 357–383.

Siren, T., Kantia, P., & Rinne, M. (2015). Considerations and observations of stress-induced and construction-induced excavation damage zone in crystalline rock. *International Journal of Rock Mechanics and Mining Sciences, 73*, 165–174.

Su, G., Feng, X., Wang, J., Jiang, J., & Hu, L. (2017). Experimental study of remotely triggered rockburst induced by a tunnel axial dynamic disturbance under true-triaxial conditions. *Rock Mechanics and Rock Engineering, 50*(8), 2207–2226.

Tao, M., Li, X., & Wu, C. (2013). 3D numerical model for dynamic loading-induced multiple fracture zones around underground cavity faces. *Computers and Geotechnics, 54*, 33–45.

Tao, M., Li, Z., Cao, W., Li, X., & Wu, C. (2019). Stress redistribution of dynamic loading incident with arbitrary waveform through a circular cavity. *International Journal for Numerical and Analytical Methods in Geomechanics, 43*(6), 1279–1299.

Tao, M., Luo, H., Wu, C., Cao, W., & Zhao, R. (2023a). Dynamic analysis of the different types of elliptic cylindrical inclusions subjected to plane SH-wave scattering. *Mathematical Methods in the Applied Sciences, 46*(2), 2773–2800.

Tao, M., Xiang, G. L., Zhao, R., & Wu, C. Q. (2023b). Scattering of P-wave and transient response around a fluid-filled cavity in an elastic medium. *Journal of Central South University, 30*(2), 568–583.

Tao, M., Zhao, H. T., Li, Z. W., & Zhu, J. B. (2020a). Analytical and numerical study of a circular cavity subjected to plane and cylindrical P-wave scattering. *Tunnelling and Underground Space Technology, 95*, 103143.

Tao, M., Zhao, R., Du, K., Cao, W., & Li, Z. (2020b). Dynamic stress concentration and failure characteristics around elliptical cavity subjected to impact loading. *International Journal of Solids and Structures, 191–192*, 401–417.

Tsang, C.-F., Bernier, F., & Davies, C. (2005). Geohydromechanical processes in the Excavation Damaged Zone in crystalline rock, rock salt, and indurated and plastic clays—in the context of radioactive waste disposal. *International Journal of Rock Mechanics and Mining Sciences, 42*(1), 109–125.

Xu, L., Gong, F. Q., & Liu, Z. X. (2022). Experiments on rockburst proneness of pre-heated granite at different temperatures: Insights from energy storage, dissipation and surplus. *Journal of Rock Mechanics and Geotechnical Engineering, 14*(5), 1343–1355.

Xu, P., Xia, T.-D., & Han, T.-C. (2006). Scattering of elastic wave by a cylindrical shell deeply embedded in saturated soils. *Acta Seismologica Sinica, 19*(2), 191–198.

Yan, P., Lu, W.-B., Chen, M., Hu, Y.-G., Zhou, C.-B., & Wu, X.-X. (2015). contributions of in-situ stress transient redistribution to blasting excavation damage zone of deep tunnels. *Rock Mechanics and Rock Engineering, 48*(2), 715–726.

Yi, C. P., Lu, W. B., Zhang, P., Johansson, D., & Nyberg, U. (2016). Effect of imperfect interface on the dynamic response of a circular lined tunnel impacted by plane P-waves. *Tunnelling and Underground Space Technology, 51*, 68–74.

Yin, T., Yang, Z., Wu, Y., Tan, X., & Li, M. (2022). Experimental investigation on the effect of open fire on the tensile properties and damage evolution behavior of granite. *International Journal of Damage Mechanics, 31*(8), 1139–1164.

Zhao, R., Tao, M., Wu, C. Q., Wang, S. F., & Zhu, J. B. (2023a). Spallation damage of underground openings caused by excavation disturbance of adjacent tunnels. *Tunnelling and Underground Space Technology, 132*, 104892.

Zhao, R., Tao, M., Zhao, H. T., Wu, C. Q., & Cao, W. Z. (2023b). Theoretical study on dynamic stress redistribution around circular tunnel with different unloading paths. *Computers and Geotechnics, 163*, 105737.

Zhou, Z. L., Wang, P. Y., Cai, X., & Cao, W. Z. (2023). Influence of water content on energy partition and release in rock failure: implications for water-weakening on rock-burst proneness. *Rock Mechanics and Rock Engineering, 56*, 6189–6205.